

PAPER

[View Article Online](#)
[View Journal](#) | [View Issue](#)

A mesoscopic model for the rheology of soft amorphous solids, with application to microchannel flows

Alexandre Nicolas and Jean-Louis Barrat[§]*

Received 26th April 2013, Accepted 18th June 2013

DOI: 10.1039/c3fd00067b

We have studied a mesoscopic model for the flow of amorphous solids. The model is based on key features identified at the microscopic level, namely periods of elastic deformation interspersed with localised rearrangements of particles that induce long-range elastic deformations. These long-range deformations are derived following a continuum mechanics approach, in the presence of solid boundaries, and are included in full in the model. Indeed, they mediate spatial cooperativity in the flow, whereby a localised rearrangement may lead a distant region to yield. In particular, we have simulated a channel flow and found manifestations of spatial cooperativity that are consistent with published experimental observations for concentrated emulsions in microchannels. Two categories of effects are distinguished. On the one hand, the coupling of regions subject to different shear rates, for instance, leads to finite shear rate fluctuations in the seemingly unsheared “plug” in the centre of the channel. On the other hand, there is convincing experimental evidence of a specific rheology near rough walls. We discuss the diverse possible physical origins for this effect, and we suggest that it may be associated with the bumps of particles into surface asperities as they slide along the wall.

1 Introduction

The flow of simple fluids can be described microscopically as a succession of local, independent processes: collisions in the kinetic theory or hopping events in the classical Eyring description. As the temperature is lowered, or as the density increases, these processes tend to become more collective, with a dynamical length scale that increases as the glass transition is approached.^{1,2} Eventually, the liquid falls out of equilibrium and acquires a non-zero shear modulus on any finite time scale, as well as a yield stress that must be overcome in order to initiate the flow. Similar changes take place in athermal materials when the jamming point is crossed following an increase in density. It is now quite well established³

Laboratoire Interdisciplinaire de Physique, Université Grenoble-Alpes, CNRS UMR 5588, BP 87, 38402 Saint-Martin d'Hères, France

that the flow mechanisms of such amorphous solids are different in essence from those of liquids, as they involve elastic interactions (shear waves) that are transmitted through solids, but not through fluids. This results in non-local effects in the flow of soft jammed/glassy materials, in contrast with the case of a simple fluid.

In fact, the flow of these materials bears notable similarities with the dynamics of earthquakes,⁴ in that it features a solid-like behavior at rest and local yielding above a given applied stress. Yielding is characterized by the emergence of local 'shear transformations' involving a few particles,⁵ associated with a local fluidisation of the material. These structural rearrangements, hereafter named plastic events and also often referred to as shear transformations or shear transformation zones in the literature, induce long-range deformations. The microscopic details vary to some extent with the particular nature of the material. In the case of foams, they are identified as T1 events, in which the local change of the first neighbors is mediated by an unstable stage with four bubbles sharing one vertex. In colloidal pastes and in atomic systems, they involve relative displacements of limited magnitude within a small group of atoms, which lead to a new equilibrium configuration that is related to the original one by a shear deformation. In all cases, the stress that was originally supported by the particles partaking in the plastic event is transmitted to the surrounding medium, which behaves as an elastic continuum. The robustness of the above scenario for an extremely wide range of materials is striking. Ample evidence of the local plastic events and their long-range effects is indeed provided both by experiments using diverse materials and simulations.^{6–8}

In the last two decades the modelling of flow in amorphous systems has evolved along two distinct, but related, lines. First, several models have been proposed that incorporate the flow scenario in an average description. Among these, the shear transformation zone⁹ and the Soft Glassy Rheology (SGR)^{10,11} models are the most sophisticated examples. Other simplified models falling into the same category are the fluidity model¹² or the very simple λ -model,¹³ which describe the average evolution of a population of flow defects under an imposed strain rate in a mean-field-like manner. The effect of the elastic interactions between these defects is not directly accounted for, but is included in the models indirectly *via* the introduction of parameters such as an effective temperature associated with the mechanical noise. These approaches have been remarkably successful in describing at least some aspects of steady state flow curves, *e.g.*, the existence of a yield stress and the low shear rate behaviour, as well as transient or oscillatory responses in various systems, from metallic glasses to foams or colloidal pastes. However, due to their intrinsic mean-field nature, fluctuations and spatial correlations in the flow are discarded. Also, in their most simplified version they are unable to account for heterogeneities and strain localisation. To capture the latter phenomenon, extensions of the models have introduced the coupling of the mean-field description and the diffusive behaviour of the effective temperature, which again can be understood as a consequence of the non-local interactions between elementary flow events.^{14–16}

An alternative line of modelling consists in implementing numerically the scenario of plastic events interacting through an elastic continuum in the form of a discrete lattice model. Such an approach was pioneered by Chen, Bak and Obukhov, in a model initially proposed for the description of earthquakes,¹⁷ and by Argon and Bulatov.^{18–20} A number of similar mesoscopic models based on the

same physical scenario, but with different implementations, have been proposed and studied in the literature.^{21–23} The models are able to produce flow curves sharing similarities with those observed experimentally, although significant differences are revealed by closer inspection; they can account for the strain localisation and its dependence on the local dynamical rules,^{23,24} and allow one to explore the influence of parameters such as ageing or temperature. They also reproduce the dynamical heterogeneities observed in the flow, and their variation with the strain rate.²⁵ However, these comparisons have generally remained qualitative, since the models are in general rather schematic, ignoring in particular tensorial aspects or convection.

In this contribution, we present a detailed study of a mesoscopic model that incorporates these elements in a manner that allows a comparison with experimental data obtained in simple geometries. In particular, we will focus on the channel flow geometry and show that the model captures experimental observations, including fluctuations in the local shear rates arising even in seemingly quiescent regions. Such fluctuations are the hallmark of non-locality and spatial cooperativity in the flow, which can give rise to spectacular long-range fluidisation phenomena.

Section 2 introduces the continuum mechanics-based description of a plastic event and presents our mesoscopic model. Details of its numerical implementation are also provided. In Section 3, we fit the parameters of the model to experimental data for concentrated emulsions taken from the literature, and we present the general features observed in our numerical simulations of a channel flow. The last two sections focus on the manifestations of spatial cooperativity in this particular geometry: Section 4 tackles cooperativity in the bulk, whereas some aspects of the specific rheology near a wall are addressed in Section 5. A shorter account of some of these results has been described in ref. 26.

2 Continuum mechanics-based description of plastic events and presentation of the mesoscopic model

Under homogeneous driving conditions, simple fluids flow homogeneously. Amorphous solids, on the other hand, exhibit localised plastic events when they are forced to flow,^{5,6,27–29} associated with local shear transformations. In this section, we use an approach rooted in continuum mechanics to describe the effect of a plastic event on the surrounding (elastic) medium, along with its time evolution. Then, we show how these results are integrated into a mesoscopic model. The presentation of the model is brought to completion by the choice of the relevant probabilities for the onset and end of a plastic event. This section is a detailed extension of previous reports.^{22,26}

2.1 Description of a plastic event

Consider a rectangular system described by Cartesian coordinates (x, y) , where $x \in [0, L_x]$ and $y \in [0, L_y]$ are the streamwise and crosswise coordinates, respectively. Should the system be unbound, the following results will be applicable provided that $L_x \rightarrow \infty$ and $L_y \rightarrow \infty$. For the time being, periodic boundary conditions are assumed.

On account of the solidity of the material (which is preserved at low shear rates), the response of the system to a perturbation can be modelled by Hooke's

law, whereby the local elastic stress σ^{el} is related to the local (deviatoric) strain ε via $\sigma^{\text{el}} = \mathbf{C}\varepsilon$, where \mathbf{C} is the stiffness matrix. Before a perturbation (here, a plastic event) sets in, the mechanical equilibrium requires that:

$$\nabla \cdot (\mathbf{C}\varepsilon^{(0)}) - \nabla p^{(0)} = 0, \quad (1)$$

where p is the pressure, and the (0) superscripts denote the initial state. In the following, the material will be considered incompressible, which implies that the displacement field u obeys $\nabla \cdot u = 0$, and isotropic, so that the elastic stress can be written, in condensed notation, as

$$\sigma^{\text{el}} = \mu \begin{pmatrix} \varepsilon_{xx} - \varepsilon_{yy} & 2\varepsilon_{xy} \\ \varepsilon_{yy} - \varepsilon_{xx} & 2\varepsilon_{xy} \end{pmatrix} = 2\mu \begin{pmatrix} \varepsilon_{xx} & -\varepsilon_{xx} \\ -\varepsilon_{xx} & \varepsilon_{xx} \end{pmatrix} \equiv 2\mu\varepsilon, \quad (2)$$

where μ is the shear modulus.

Clearly, Hooke's law will only hold within a certain limit. Indeed, when the configuration is too strained locally, say, in a region $\mathcal{S}^{(0)}$, the particles rearrange so that the system is brought to a new local minimum: this is a plastic event. While this rearrangement occurs, the memory of the reference elastic configuration is lost, and, consequently, the local elastic stress vanishes. The region undergoing the rearrangement is therefore liquid-like and its stress will be mainly of dissipative origin. Following this line of thinking and neglecting inertia, the force equilibrium during the plastic rearrangement reads

$$\begin{cases} \nabla \cdot \sigma^{\text{diss}} - \nabla p = 0 & \text{in region } \mathcal{S}, \\ 2\mu \nabla \cdot \varepsilon - \nabla p = 0 & \text{outside region } \mathcal{S}. \end{cases} \quad (3)$$

Notice that the boundaries of the plastic region shall be deformed during the event and \mathcal{S} refers to the deformed region. In eqn (3), the dissipative stress σ^{diss} was supposed to be mainly concentrated in the rearranging region. For simplicity, we further assumed that the dissipation is linear with respect to the strain rate, viz. $\sigma^{\text{diss}} = 2\eta_{\text{eff}}\dot{\varepsilon}$. This linearity is naturally to be understood as a simplification, and not as a claim of the existence of some universality regarding the dissipative mechanism (see ref. 30 for a non-linear law in the case of a foam). In addition to eqn (3), the force balance requires the continuity of the stress all along the boundary of region \mathcal{S} . If \mathcal{S} is small enough so that the (plastic) deformation rate in this region can be considered homogeneous, viz., $\dot{\varepsilon}(r) \equiv \dot{\varepsilon}^{\text{pl}}$ for $r \in \mathcal{S}$, the continuity of the stress all along the boundary $\partial\mathcal{S}$ of the plastic inclusion leads to:

$$\dot{\varepsilon}^{\text{pl}} = \frac{1}{\tau} \varepsilon_{\partial\mathcal{S}}, \quad (4)$$

where $\varepsilon_{\partial\mathcal{S}}$ refers to the (elastic) strain on the outer boundary $\partial\mathcal{S}$. The time scale $\tau \equiv \frac{\eta_{\text{eff}}}{\mu}$ for the viscous dissipation of the elastic energy has been made apparent.

The leading-order response of the system to the plastic event immediately follows from eqn (4): it simply comes down to a (plastic) strain rate $\dot{\varepsilon}^{\text{pl}}(t) = \frac{1}{\tau} \varepsilon_{\partial\mathcal{S}}^{(0)}$ affecting only region \mathcal{S} . In an unconstrained environment, the inclusion would therefore undergo a deformation $\varepsilon^{(1)}dt$ in a time interval dt .

However, since the inclusion is embedded in a solid, the latter reacts to this plastic strain: supplementary elastic stress and pressure fields, $\dot{\sigma}^{(1)}dt = 2\mu\dot{\varepsilon}^{(1)}dt$ and $\dot{p}^{(1)}dt$ respectively, are thereby induced in the medium.[†] The derivation of the fields $\dot{\sigma}^{(1)}$ and $\dot{p}^{(1)}$ is presented in the next subsection. For the time being, let us remark that, thanks to the linearity of the equations, one can express the induced stress on the boundary $\partial\mathcal{S}$ as

$$\dot{\sigma}_{\partial\mathcal{S}}^{(1)} = 2\mu\mathcal{G}_0\dot{\varepsilon}^{\text{Pl}}, \quad (5)$$

where \mathcal{G}_0 is a yet unknown tensor. Now, since the response of the solid is a reaction to an imposed shear strain $\dot{\varepsilon}^{(1)}dt$, it will oppose it, at least in the direct vicinity of the inclusion. Therefore, one expects the eigenvalues of \mathcal{G}_0 to be negative. Inserting eqn (2) and (4) into eqn (5) yields, after simplification:

$$\dot{\varepsilon}_{\partial\mathcal{S}}^{(1)}(t) = \frac{\mathcal{G}_0}{\tau}\varepsilon_{\partial\mathcal{S}}(t) \quad (6)$$

Eqn (6) expresses the fact that, up to a (potentially time-dependent) shape prefactor \mathcal{G}_0 , the force driving the rearrangement is the elastic stress imposed on \mathcal{S} by the rest of the system, and that, in opposing this force, dissipation sets a finite timescale τ to this plastic transformation.[‡] Cloitre *et al.*³² suggested that the duration of a rearrangement in soft colloidal pastes coincides with the shortest structural relaxation time τ_β , which also results from a “competition between elastic restoring forces and interparticle friction”, and experimentally confirmed the proposed scaling $\frac{\eta_{\text{eff}}}{\mu}$ for the latter time (where η_{eff} is determined by the dissipation within lubrication films). This scaling was also used to collapse flow curves onto a single master curve, which bolsters its relevance for the rheology of these materials.

2.2 Calculation of the elastic deformation induced by a single plastic event (2D, tensorial)

Ref. 33 proposed a method to derive the fields $\dot{\varepsilon}^{(1)}dt$ and $\dot{p}^{(1)}dt$ induced by the plastic strain $\dot{\varepsilon}^{\text{Pl}}dt$, in a simplified context. First, one considers the limit of an infinitely small plastic inclusion \mathcal{S} , $\varepsilon^{\text{Pl}}(r) \rightarrow \varepsilon^{\text{Pl}}a^2\delta(r-r_0)$, where r_0 is the centre of region \mathcal{S} , and a , the typical linear size of \mathcal{S} . (The dots indicating derivation w.r.t. time are omitted in this section). Secondly, by virtue of the linearity of the equations, the inclusion applies a stress $\sigma^{\text{inc}} = 2\mu\alpha\varepsilon^{\text{Pl}}$ on its surrounding, where α is a scalar (instead of a tensor) because of symmetry arguments. At the expense of a renormalisation of the timescale τ appearing in the definition of $\dot{\varepsilon}^{\text{Pl}}$, eqn (4), *viz.* $\tau \equiv \alpha^{-1}\frac{\eta_{\text{eff}}}{\mu}$, we can consider that $\alpha = 1$. The mechanical equilibrium in the solid then reads:

$$2\mu\nabla\cdot[\varepsilon^{(1)}] - \nabla p^{(1)} = 2\mu\nabla\cdot[\varepsilon^{\text{Pl}}a^2\delta(r-r_0)] \quad (7)$$

[†] This deformation will, in turn, affect the plastic deformation rate $\dot{\varepsilon}^{\text{Pl}}$, but these higher order effects are neglected here.

[‡] The finite duration of a plastic rearrangement, which is neglected in the Soft Glassy Rheology model,¹⁰ the Kinetic Elastoplastic model,¹⁶ as well as in the mesoscopic models of ref. 21,23, may play a crucial role in the compressed exponential relaxation of different soft materials. For details, see ref. 31.

To pursue, eqn (7) is solved with the help of the Oseen–Burgers tensor O , expressed in Fourier coordinates $\underline{q} \equiv (p_m, q_n)$, where $p_m \equiv \frac{2\pi m}{L_x}$ and $q_n \equiv \frac{2\pi n}{L_y}$, with $m, n \in \mathbb{Z}$:

$$\hat{O}(\underline{q}) = \frac{1}{\mu \underline{q}^2} \left(1 - \frac{1}{\underline{q}^2} \underline{q} \otimes \underline{q} \right). \quad (8)$$

The Oseen–Burgers tensor is the elementary solution in terms of the displacement u of the equations $\{2\mu \nabla \cdot \varepsilon - \nabla p = \delta(r), \nabla \cdot u = 0\}$, where the linearised deformation tensor obeys $\varepsilon = \frac{\nabla u + (\nabla u)^T}{2}$, with the boundary conditions specified above. Therefore,

$$u^{(1)}(\underline{q}) = 2\mu \hat{O}(\underline{q}) \cdot (-i \underline{q} \cdot \hat{\varepsilon}^{\text{pl}}). \quad (9)$$

Recalling Hooke's law, $\hat{\sigma}^{(1)}(\underline{q}) = 2\mu \left[i \frac{\underline{q} \otimes u^{(1)} + (\underline{q} \otimes u^{(1)})^T}{2} - \hat{\varepsilon}^{\text{pl}}(\underline{q}) \right]$, one finally arrives at:

$$\begin{pmatrix} \hat{\varepsilon}_{xx}^{(1)} \\ \hat{\varepsilon}_{xy}^{(1)} \end{pmatrix}(\underline{q}) = \hat{\mathcal{G}}^\infty(\underline{q}) \cdot \begin{pmatrix} \hat{\varepsilon}_{xx}^{\text{pl}} \\ \hat{\varepsilon}_{xy}^{\text{pl}} \end{pmatrix}(\underline{q}) \quad (10)$$

where the elastic propagator $\hat{\mathcal{G}}^\infty$ obeys:

$$\hat{\mathcal{G}}^\infty(\underline{q}) \equiv \frac{1}{\underline{q}^4} \begin{bmatrix} -(p_m^2 - q_n^2)^2 & -2p_m q_n (p_m^2 - q_n^2) \\ -2p_m q_n (p_m^2 - q_n^2) & -4p_m^2 q_n^2 \end{bmatrix}. \quad (11)$$

Eqn (10) and (11) express the elastic deformation field induced by a pointlike plastic event in a system with periodic boundary conditions. The corresponding stress field is straightforwardly obtained by multiplication with the shear modulus 2μ .

In real space, the propagator expressed in eqn (11) has a four-fold angular symmetry and decays as r^{-d} , where $d = 21$ is the spatial dimension. These properties are consistent with observations from atomistic simulations^{6,28,34} as well as experiments.³⁵

Note that the present treatment does not describe the dilational effects³⁶ possibly taking place during plastic events. These effects may naturally add quantitative corrections to the picture drawn here, but, along with the associated flow concentration coupling³⁷ and the free volume diffusion mechanisms (see ref. 14 and references therein), they are probably not of paramount importance in the high density–low temperature situations considered here,³⁸ where such effects are not always present.^{39,40}

2.3 Implementation of parallel confining walls

In order to study a genuine channel geometry, the boundary conditions need to be adapted to take into account two infinite parallel walls, directed along e_x , bounding the flow, while keeping the periodicity in the e_x direction. The effect of the walls is modelled by imposing no-slip boundary conditions at their locations, in line with what is commonly done in fluid mechanics.

To implement the no-slip boundary conditions, we extended the treatment in ref. 33: the system is duplicated in the direction perpendicular to the walls, so that the region $y \in [0, L_y]$ describes the real system, while the region $y \in [-L_y, 0]$ is fictitious. For each plastic event (in the real system), a symmetric 'image plastic event' is created in the fictitious region (Fig. 2). The y -component of the velocity field is thereby cancelled at the walls. To remove the x -component of the velocity, adequate forces directed along e_x are added along the walls. These (fictitious) forces add a corrective term $\hat{\varepsilon}^{\text{corr}}$ to the deformation field $\hat{\varepsilon}^\infty$ obtained for the periodic boundary:

$$\hat{\varepsilon}(\underline{q}) = \hat{\varepsilon}^\infty(\underline{q}) + \hat{\varepsilon}^{\text{corr}}(\underline{q}).$$

The calculation of $\hat{\varepsilon}^{\text{corr}}(\underline{q})$ is presented in Appendix A and yields the following result:

$$\begin{pmatrix} \hat{\varepsilon}_{xx}^{\text{corr}}(p_m, q_n) \\ \hat{\varepsilon}_{xy}^{\text{corr}}(p_m, q_n) \end{pmatrix} = \begin{pmatrix} \frac{-2p_m q_n^2}{q^4} \left[i \sum_y \zeta_\delta(X) \mathcal{F}_x \varepsilon_{xy}^{\text{pl}}(p_m, y) + 2 \sum_y \xi_\delta(X) \mathcal{F}_x \varepsilon_{xx}^{\text{pl}}(p_m, y) \right] \\ \frac{q_n(p_m^2 - q_n^2)}{q^4} \left[i \sum_y \zeta_\delta(X) \mathcal{F}_x \varepsilon_{xy}^{\text{pl}}(p_m, y) + 2 \sum_y \xi_\delta(X) \mathcal{F}_x \varepsilon_{xx}^{\text{pl}}(p_m, y) \right] \end{pmatrix}, \quad (12)$$

where \sum_y denotes an integral over all the streamlines $y = \text{cst}$ and \mathcal{F}_x indicates a Fourier transformation along the x -direction. X is used as a shorthand for $\left(\frac{\pi y_{\text{ev}}}{L_y}, \frac{p_m L_y}{\pi}\right)$ and the analytical expressions of the functions $\zeta_\delta(X)$ and $\xi_\delta(X)$ can be found in Appendix A. In Fig. 4, the displacement field induced by a single plastic event is depicted to illustrate the result of the calculation.

Note that the corrective term couples the different Fourier modes so that the translation invariance of the propagator \mathcal{G} is broken (in the y -direction). In particular, for a given plastic strain, the local strain response now depends upon the distance to the wall. The dependence on the distance for a plastic event $\{\varepsilon_{xx}^{\text{pl}} = 0, \varepsilon_{xy}^{\text{pl}} \neq 0\}$ is presented in Fig. 3 for a system that is coarse-grained into blocks of unit size (see next section). In particular, one can see that the local strain relaxation induced by a given plastic strain is around 35% higher in the direct vicinity of a wall than in the bulk case, owing to the vicinity of a solid boundary.

2.4 Dynamics of the model and space discretisation

At every point in space, the dynamics is governed by the following equation, including both the external driving $\dot{\Sigma}^{\text{ext}}$ and the (local and non-local) stress redistribution due to plastic events:

$$\partial_t \sigma(r) = \dot{\Sigma}^{\text{ext}}(r) + \int \mathcal{G}(r, r') \cdot 2\mu \dot{\varepsilon}^{\text{pl}}(r') d^2 r', \quad (13)$$

where $\dot{\varepsilon}^{\text{pl}}(r) = \frac{\sigma(r)}{2\mu\tau}$ if r is in a plastic region, $\dot{\varepsilon}^{\text{pl}}(r) = 0$ otherwise, and the propagator \mathcal{G} takes into account both the bulk (periodic) contribution and the corrections due to the presence of walls. The plastic activity is determined by checking

at every time step and at every point in space, the elements that undergo a plastic event. The criterion for triggering plastic events will be discussed in the next section. The time derivative in eqn (13) is handled numerically with a Eulerian procedure, with time step $dt \leq 0.01\tau$.

The convolution part of eqn (13) is most easily solved in the Fourier space, where the convolution turns into a product involving the propagator derived previously (see eqn (11) and (13), for the two contributions to \mathcal{G}). To prepare the use of a Fast Fourier Transform routine, the system is spatially coarse-grained into a rectangular lattice of square-shaped blocks of unit size. Physically, the size of the blocks should correspond to the spatial extent of a plastic event.

Technically, the slow decay of $\hat{\sigma}_{xx}(q)$ with q generates some irregularities in the computation of the associated back-Fourier transform. Accordingly, for the sake of precision, we used a finer mesh for the computation of the Fourier transformations, *i.e.*, we divided each block into four subblocks, so that each plastic event now spans four subblocks. Thanks to this technical trick, a smooth stress field is obtained, as shown in Fig. 1.

Besides, the mechanical equilibrium requires the average of the shear stress over any streamline (or any line with a given direction) to be homogeneous. However, the assumption of pointwise plastic events combined with the discretisation of space is not entirely consistent, insofar as it results in moderate violations of the aforementioned homogeneity, when plastic events are far off the direction of macroscopic shear. In order to restore homogeneity, an *ad hoc* shear stress is added globally to every streamline. We have checked that this procedure has very little effect on the results presented below.

2.5 Coarse-grained convection

Although the presence of a lattice precludes a rigorous implementation of convection, a coarse-grained version can be introduced as follows: the average velocity of each streamline in the flow direction is rigorously calculated at each time step, *viz.*

$$\begin{aligned} \langle u_x \rangle_x(y_0) &\equiv \frac{1}{L_x} \int_{-L_x/2}^{L_x/2} u_x(x, y_0) dx \\ &= \sum_{y_{ev}} \left[\text{sign}(y_0 - y_{ev}) \cdot \left(1 - \frac{|y_0 - y_{ev}|}{L_y} \right) + 1 - \frac{y_{ev}}{L_y} - \frac{y_0}{L_y} \right] \mathcal{F}_x e_{xy}^{\text{pl}}(m=0, y_{ev}). \end{aligned}$$

Details of the algebra are provided in Appendix B. The line displacement can thus be updated at each time step. Whenever the displacement on a line grows larger than a multiple of the unit block size, this line incrementally shifts the adequate number of units, as a whole. In so doing, the regularity of the lattice is preserved.

A technical detail might be worth mentioning: a naïve implementation of the above method results in a violation of the Galilean invariance, insofar as lines with lower velocity will be shifted less often than others (artificial pinning) and therefore will tend to conserve their neighbours (in the velocity gradient direction) for a longer time, whereas the motion with respect to neighbouring lines should be exclusively controlled by the local shear rate. It turns out that, in a simple shear situation, the system is quite sensitive to such a bias, which may lead

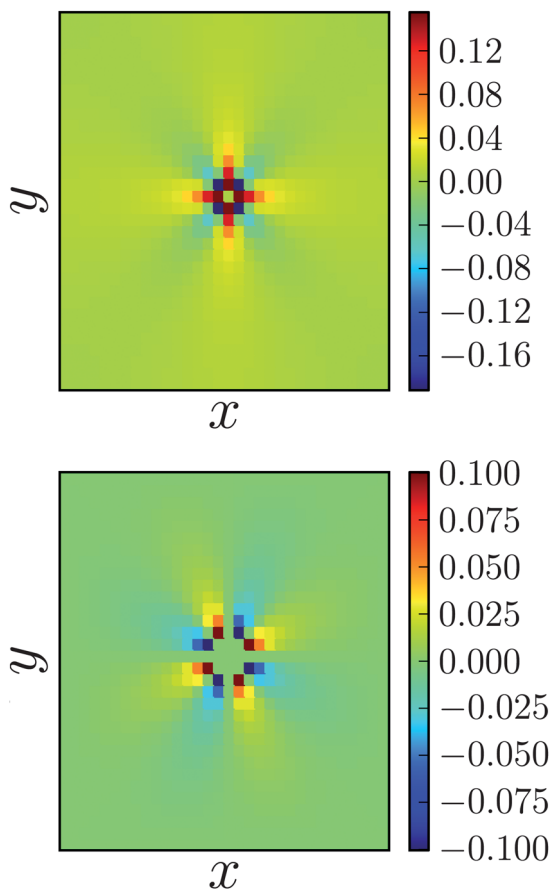


Fig. 1 Deformation field $\epsilon^{(1)}$ induced by a single plastic event ϵ_{xy}^{pl} . Top: $\epsilon_{xy}^{(1)}$ component; bottom: $\epsilon_{xx}^{(1)}$ component. The values are normalised by the absolute value of the locally induced deformation $\epsilon_{xy}^{(1)}$. Because of the comparatively large (in magnitude) peak value at the origin, the central block has been artificially coloured.

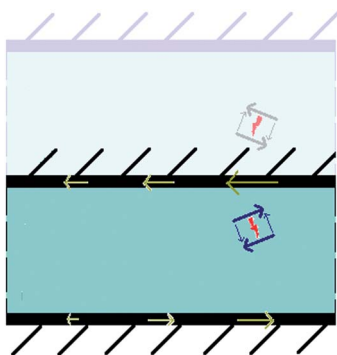


Fig. 2 Sketch of the duplicated system.

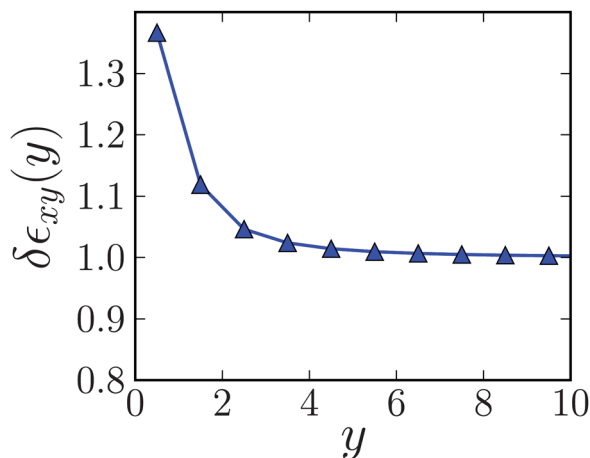


Fig. 3 Decrease of the local elastic strain $|\epsilon_{xy}^{(1)}|$ induced by a given plastic strain ϵ_{xy}^p as a function of the distance y to the wall (expressed in block units, which is the only relevant length scale). Values have been normalised to the 'bulk' value, that is, the quantity measured infinitely far from the wall.

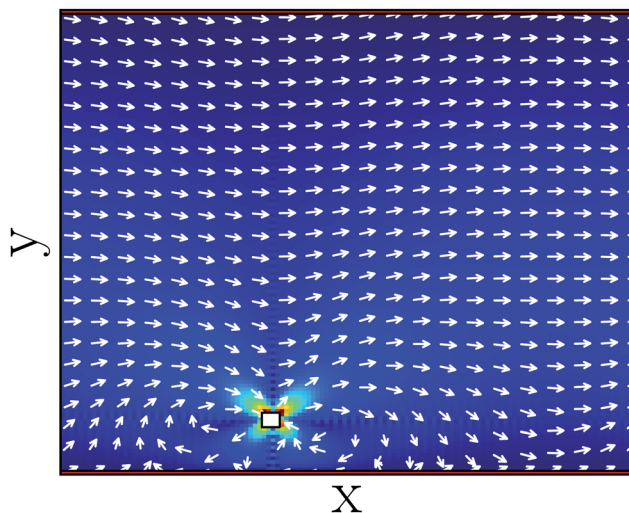


Fig. 4 Displacement field induced by a single plastic event (located in the white square). The white arrows show the direction of the field, while the colour code represents the displacement amplitude (brighter colours indicate higher amplitude). Walls, drawn as red lines, are present at the top and at the bottom of the system.

'pinned' lines to concentrate more plastic activity. The practical solution to this issue consists in adding a random offset displacement to all streamlines, so that no artificial pinning can occur.

2.6 Probabilities for the onset and end of a plastic event

So far, we have quantitatively described the effect of a plastic event and detailed its derivation from rather well established principles. In order to complete the

model, criteria must now be fixed with regard to the onset and termination of a plastic event. Since the mesoscopic model is oblivious to the microscopic arrangement of the particles and their stability, the criteria will obviously be somewhat arbitrary. In the present model, they will involve two rates, $l(\sigma)$ and $e(\sigma)$, which govern, respectively, the transition from the elastic to the plastic regime and the recovery of elastic behavior after initiation of the plastic event,

$$\text{elastic regime} \xrightleftharpoons[e(\sigma)]{l(\sigma)} \text{plastic event.}$$

The use of rates introduces a simple element of stochasticity in the model, and indirectly accounts for the variability of local environments.

Let us consider a mesoscopic region susceptible to undergo a plastic rearrangement. In the elastic regime, its configuration minimises the potential energy, under the stress/strain constraints imposed at the boundaries by the rest of the material. The minimum is stable as long as $E - E_{\text{constraint}} \leq E_a$, where we assume the existence of an average energy barrier E_a . In an Eyring-like type of approach, the constraint is expressed as: $E_{\text{constraint}} \propto \sigma$, where σ is the local stress applied by the outer region, and we take an activation volume equal to unity. Consequently, the rate of plastic activation depends exponentially on the local stress. In the following discussion, we will use the expression

$$l(\sigma) = \Theta(\sigma - \sigma_{\mu y}) \exp\left(\frac{\sigma - \sigma_y}{x_{\text{loc}}}\right) \tau^{-1}.$$

Three parameters have been introduced in this expression: σ_y is the yield stress associated to the average energy barrier; x_{loc} is a material-dependent activation temperature. Unlike the effective temperatures used in the Soft Glassy Rheology model or the Eyring-like stress fluctuation approach,⁴¹ x_{loc} only accounts for local microscopic effects and does not include the local stress fluctuations due to stress redistribution, *i.e.*, the mechanical noise: the latter should emerge naturally as a consequence of long range interactions between events, within the framework described above. Note that the limit $x_{\text{loc}} \rightarrow 0$ of the activation rate coincides with the usual von Mises yielding criterion, which states that the material yields if and only if $\sigma \geq \sigma_y$. However, under shear stress, the effective lowering of the energy barriers results in the necessity to preserve the possibility of activated events, even in materials usually referred to as athermal at rest. For instance, the occurrence of rearrangements in granular matter long after shear cessation supports this claim,⁴² although the physical reason for such rearrangements is far from clear. Another possible justification for introducing x_{loc} may be that it effectively accounts for some dynamical disorder in the local yield stress. Finally, we found that introducing this fluctuating, apparently activated character in the yield criterion is the only way to obtain flow curves in reasonable agreement with experimental data, as shown below.

The parameter $\sigma_{\mu y}$ in the Heaviside function Θ is a critical stress, intended to be small ($\sigma_{\mu y} \ll \sigma_y$) and below which no rearrangement can occur. Clearly, this is an *ad hoc* approach to conserve a finite macroscopic yield stress in the limit of a vanishing shear rate $\dot{\gamma}_{\text{app}} \rightarrow 0$, when no ageing process is explicitly taken into account. Note that Amon *et al.*,⁴³ in a paper investigating the behaviour of

granular matter on a tilted plane, recently called for a model displaying two critical stresses, with a microfailure stress in addition to the macroscopic one, although with a distinct definition.

A plastic event lasts until the local configuration gets trapped in a new potential well. This trapping is expected to occur when the local energy reaches low enough values, or, equivalently (recall that $\sigma^{\text{diss}} \propto 2\mu\varepsilon_{\partial\mathcal{V}}$, see eqn (4)), when the dissipative stress is dominated by the local elastic stress (which was neglected in eqn (4)). Consequently, we define an associated threshold for the recovery of the elastic stability, whose value is set to $\sigma_{\mu y}$ in order to limit the number of parameters. The introduction of a new intensive parameter x_{res} allows us to write the rate at which elastic behaviour is recovered as: $e(\sigma) = \exp\left(\frac{\sigma_{\mu y} - \sigma}{x_{\text{res}}}\right)\tau^{-1}$.

The definition of the rates e and l completes the description of the model. At each time step, the probability of failure of an elastic element is $l(\sigma)dt$, while the probability that a plastic element becomes elastic again is $e(\sigma)dt$.

3 Fitting of model parameters and general observations in a channel flow

In order to test the validity of the mesoscopic model presented in the previous section, we started fitting the model parameters by comparing the flow curve obtained in simulations of a simple shear setup to the experimental results for a concentrated emulsion.

3.1 Fitting of model parameters

We use units of time and stress such that $\tau = 1$ and $\sigma_y = 1$, and we set $\frac{\mu}{\sigma_y} = 1$ (note that the value of $\frac{\mu}{\sigma_y} = 1$ only contributes to rescaling the shear rate if the convection is omitted). The model then involves three parameters, $\sigma_{\mu y}$, x_{loc} and x_{res} .

In the following, our numerical simulations are compared to the experimental data for concentrated oil-in-water emulsions collected by two different groups, Goyon *et al.*⁴⁴ and Jop *et al.*⁴⁵ The experimental systems are concentrated emulsions of 6–7 μm droplets of silicon oil in a water–glycerol mixture at an oil volume fraction $\phi \sim 0.75$ significantly larger than the jamming volume fraction. Both groups report a Herschel–Bulkley dependence of the shear stress on the shear rate, that is, $\sigma = \sigma_d [1 + (\tau_{\text{HB}}\dot{\gamma})_{\text{app}}^n]$, with an exponent $n \simeq 0.5$ in both cases.

This Herschel–Bulkley law allows us to fit the remaining model parameters. To do so, we simulated a simple shear flow by setting the driving force to $\sum_{\text{app}} = \mu\dot{\gamma}_{\text{app}}$ in eqn (13), with a stressless state as the initial condition. By varying the parameters, we find that the combination $\{\sigma_{\mu y} = 0.17, x_l = 0.249, x_e = 1.66\}$ provides a quite satisfactory fitting of the flow curve, as shown in Fig. 5. Note that the model units of time and stress have been appropriately rescaled in the figure, to allow for comparison with the experimental values. Of course, one may argue that the fitting to the flow curve only loosely constrains the parameters, implying that other combinations of parameters could yield the same result. Nevertheless, we would like to mention that, when starting with a moderately different set of parameters and after fine-tuning it to better match the data, we have recovered parameters similar to those selected.

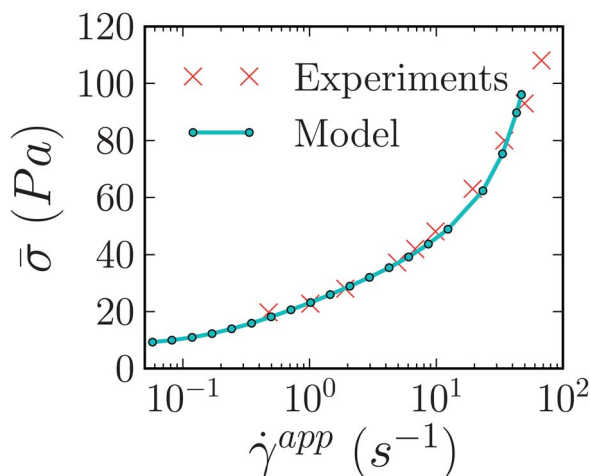


Fig. 5 Experimental (crosses) and simulated (dots) flow curves. The experimental data were obtained by Goyon *et al.* for an emulsion of $\sim 6.5 \mu\text{m}$ silicon oil droplets in a water–glycerin mixture at volume fraction $\phi = 75\%$. The solid line is a guide to the eye.

3.2 Channel flow: general observations

Having set the model, we now turn to the specific case of a channel flow. Indeed, many intriguing experimental results have been reported concerning the flow of soft jammed/glassy materials with that geometry,^{39,44–48} which is also relevant for practical applications, in particular in the area of microfluidics.

First of all, it is important to realise that, unlike the simple shear case, the flow is pressure driven in a channel flow, instead of being strain driven. Recalling that the driving \sum^{ext} in eqn (13) corresponds to the response of a purely elastic solid, it immediately follows that: $\sum^{\text{ext}} = 0$, $\sigma_{xy}(x, y, t = 0) = \nabla p \cdot (y - L_y/2)$. Note the streamline-averaged stress conserves a linear profile throughout the simulation, because plastic events induce a homogeneous streamline-averaged stress, owing to the mechanical equilibrium.

We first discuss some general features of the flow of soft jammed solids in that geometry. Conspicuous is, in the first place, the presence of a “plug” in the centre of the channel, *i.e.*, a solid-like region in which the material is convected, but not sheared. The plug can clearly be seen in Fig. 6, which demonstrates a nice agreement between the numerical and the experimental (time averaged) velocity profiles across the channel. Note that showing the velocity differences with respect to the maximal velocity across the channel obviates the experimental issue of the determination of the wall slip.

However, averaging over time masks the temporal fluctuations of the flow. If one heeds the variations of the maximal streamline velocity of the simulated flow with respect to time, flow intermittency becomes evident. § This phenomenon is more acute for narrow channels (see Fig. 8), in agreement with results from numerical simulations regarding the effect of the confinement (see ref. 40 and

§ However, these fluctuations would presumably vanish in our model if the channel were of infinite length.

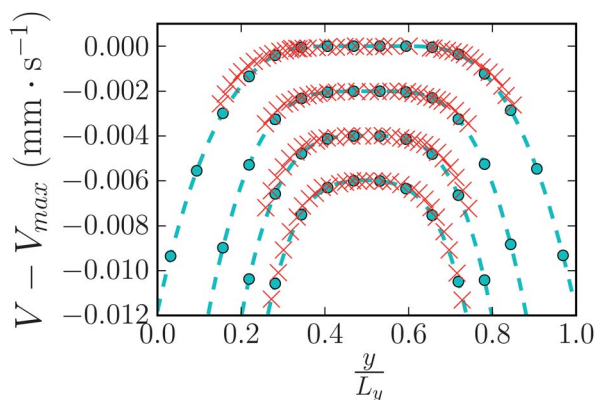


Fig. 6 Experimental (crosses) and simulated (dots) velocity profiles, for stresses at the wall $\sigma_w = 141$ Pa, 188 Pa, 235 Pa, 282 Pa, corresponding to $\sigma_w = 0.36, 0.48, 0.60, 0.72$ in model units, from top to bottom. The experimental data are courtesy of Jop *et al.*⁴⁵ The model time and stress units have been rescaled to match the experimental data.

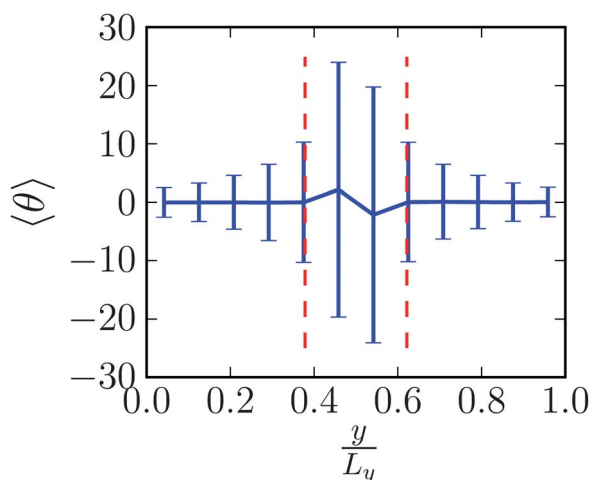


Fig. 7 Principal direction $\theta \in [-45^\circ, 45^\circ]$ of plastic events as a function of the position in the channel. Channel width: 12. $\sigma_w = 0.6$ in model units. The vertical dashed lines delimit the “plug”, *i.e.*, the region where $|\langle \sigma_{xy} \rangle| \leq \sigma_d$. The bars give the standard deviation, $\pm(\langle \theta^2 \rangle - \langle \theta \rangle^2)$.

references therein). Note that flow intermittency, or “stick-slip” behaviour, has often been reported experimentally, but it has been interpreted in various ways depending on the particular system under study: the creation and failure of force chains is put forward in the case of granular matter,^{49,50} while variations in the local concentration of colloids and erosion by the solvent have been reported for concentrated colloidal suspensions.⁴⁸

The spatial distribution of plastic events is also of interest. Indeed, although the plug remains virtually still on average, sparse plastic events are clearly seen to occur in that region, especially for narrow channels, and, consequently, below the

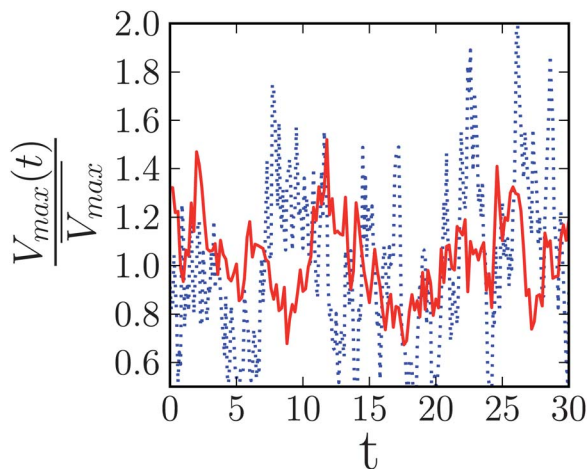


Fig. 8 Time variations of the maximal velocity in the channel, rescaled by its average value over time, for two channel widths: (solid red line) 24 blocks, (dotted blue line) 6 blocks.

bulk yield stress. Therefore, these plastic events essentially originate in cooperative effects, *via* the redistribution of stress generated by distant plastic events. Being of cooperative nature, the principal direction of their stress at the yielding point (the ‘angle of yield’ of the plastic event) is broadly dispersed, since it is not strongly biased by a fixed applied shear (see Fig. 7).

4 Cooperativity in the bulk flow: a manifestation of the coupling between heterogeneous regions

4.1 Origin and description of the non-locality in the flow

Spatial cooperativity is a hallmark of the flow of amorphous solids: because of the solidity of these materials, shear waves can propagate in the bulk. Accordingly, a plastic event induces a long-range deformation of the material and can thus set off other plastic events, possibly triggering an avalanche. However, the channel geometry is particular in that the driving is intrinsically inhomogeneous; therefore, the cooperativity couples regions (streamlines) subject to different stresses.

When considering a given region, one may then expect its behaviour to differ from what it would have in a homogeneous flow. This is a serious issue, since it undermines the paradigm that there exists a constitutive equation relating the local shear rate to the local shear stress, as explained by Goyon and colleagues.^{39,44} (Note, however, that doubts regarding the existence of a single flow curve for concentrated emulsions had also been mentioned earlier, following experiments in a different geometry.⁵¹)

To rationalise the deviations that they had observed experimentally, Goyon *et al.*³⁹ made use of a diffusion equation operating on the local fluidity, that is to say, the inverse viscosity $f(r) \equiv \frac{\dot{\gamma}(r)}{\sigma_{xy}(r)}$:

$$\xi^2 \Delta f - (f - f_{\text{bulk}}[\sigma(y)]) = 0, \quad (14)$$

where $f_{\text{bulk}}(\sigma)$ denotes the fluidity measured in a homogeneous flow at applied stress σ . The length scale ξ is a cooperative length, that scales with the particle diameter.^{39,52} This diffusion equation is based on the idea that plastically active regions will fluidise their neighbours, and inversely. In ref. 16, Bocquet *et al.* showed that this equation can formally be derived from a Hebraud–Lequeux fluidity model,¹² provided heterogeneities are taken into account. However, the limitations imposed by the analytical treatment required to cut off the propagator beyond the first neighbours, and to consider the limit of the vanishing shear rate.

Nevertheless, eqn (14) was found to provide a very satisfactory description of experimental and numerical data in several cases,^{39,40,44–46,52} provided that the parameters, that is, the cooperativity length ξ and the value f_{wall} of the fluidity at the wall, are carefully fitted.

Assuming that this equation offers a valid first-order approximation of the flow, we have used it to assess the amplitude of the expected deviations from bulk behaviour.

To do so, we quantified the extent of the coupling by estimating the relative deviation $\delta f(y) \equiv f(y) - f_{\text{bulk}}$ of the fluidity. This defines a dimensionless number, the Babel number $\text{Ba} \equiv \frac{\delta f}{f}$. In Appendix C, we show that, under the assumption of

a Herschel–Bulkley constitutive equation, Ba is of the order of $\left(\xi \frac{\|\nabla \sigma\|}{\sigma - \sigma_d} \right)^2$, that is, $\left(\xi \frac{\|\nabla p\|}{\sigma - \sigma_d} \right)^2$ for a channel flow.

Noteworthy is the (quadratic) dependence of the Babel number on the stress gradient, *i.e.*, the pressure gradient in a Poiseuille flow. Indeed, it is generally several orders of magnitude larger in microchannels than in their larger counterparts, which explains why striking manifestations of cooperativity have been observed only in the former. The Babel number is also negligible in the wide-gap Taylor–Couette geometry. For instance, a rough estimation yields $\text{Ba} \sim 10^{-9}$ at most in the wide-gap setup used by Ovarlez *et al.*⁵³ where no deviations from macroscopic rheology were reported.

The denominator of Ba, $(\sigma - \sigma_d)^2$, also deserves a comment: at high applied stresses, when the material is more fluid-like, relative deviations become less significant. We should however say that, to measure relative deviations, the absolute fluidity deviations are divided by the fluidity, which increases as σ increases.

4.2 Non-local effects in the velocity profiles

Following the above considerations, we expect deviations from macroscopic rheology to increase with confinement, at a fixed wall stress.

Indeed, Goyon's experiments on emulsions confined in microchannels with smooth walls tend to indicate that the deviations of the velocity with respect to the bulk predictions follow such a trend. However, overall, these deviations were found to be rather small. The mentioned effect of the confinement is also confirmed by Chaudhuri *et al.* with atomistic simulations of a Poiseuille flow with biperiodic boundary conditions with atomistic simulations.⁴⁰

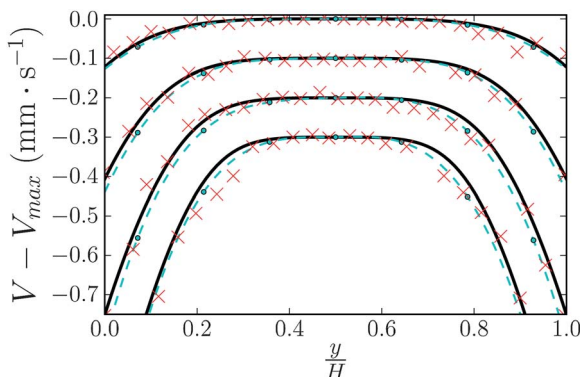


Fig. 9 Velocity profiles across the channel, for $\sigma_w = 45, 60, 75, 91$ Pa, *i.e.*, $\sigma_w = 0.75, 1.0, 1.25, 1.52$ in model units, from top to bottom: (dashed line) simulation results, (solid line) predictions based on the numerical bulk flow curve. The crosses are the experimental data obtained by Goyon *et al.*⁴⁴ Note that the curves have been shifted with respect to each other for clarity.

Fig. 9 shows a comparison between the actual velocity profile obtained with simulations of the mesoscopic model and the predictions from the (bulk) flow curve. As in the experiments, small deviations can be observed. For the extent of these deviations to roughly match that in the experiments, the channel width must be of the order of 7–10 block units. From this we deduce a first estimate for the linear size N_ϕ of a mesoscopic block in terms of particle diameters: $N_\phi \approx 2$, which is comparable to the experimental values found in the literature.³⁵

Let us now investigate how compatible our simulation results are with the fluidity diffusion equation, eqn (14). To solve eqn (14), two boundary conditions are required: for symmetry reasons, we impose $f(y=0)=f(y=L_y)$, and we set the fluidity at a point close to the wall to the value measured in the simulations. In addition, the shear-rate dependence of the cooperativity length ξ must be specified. Two possibilities are considered in Fig. 10: either, following Goyon *et al.*,³⁹ ξ is supposed independent of the shear rate, *i.e.*, $\xi = \xi_0$, or a power-law dependence is assumed, $\xi(\dot{\gamma}) = \xi_0(\dot{\gamma}\tau)^{-1/4}$, where $\dot{\gamma}$ is the product of the local shear stress and the fluidity, as derived in ref. 16 in the limit $\dot{\gamma} \rightarrow 0$, and in reasonable agreement with the data of ref. 45. In both cases, ξ_0 is adjusted by a least square minimization. Both cases give a reasonable fit, but neither matches our data accurately over the whole range of applied pressures. We ascribe this defect, among other details, to the approximation of long-range interactions by a diffusive term, and to the neglect of fluidity fluctuations.

In Fig. 11, we have assessed the predictive capability of the theoretically derived Babel number for our channel flow simulations by plotting the $\frac{\delta f}{f}$ obtained in our simulations as a function of $Ba = \left(\xi \frac{\|\nabla\sigma\|}{\sigma - \sigma_d} \right)^2$. It shows a global trend towards larger relative deviations from macroscopic rheology for larger Ba , but the correlations are poor. Nevertheless, one may expect Ba to still be a valid predictor in practice, when widely different situations are considered.

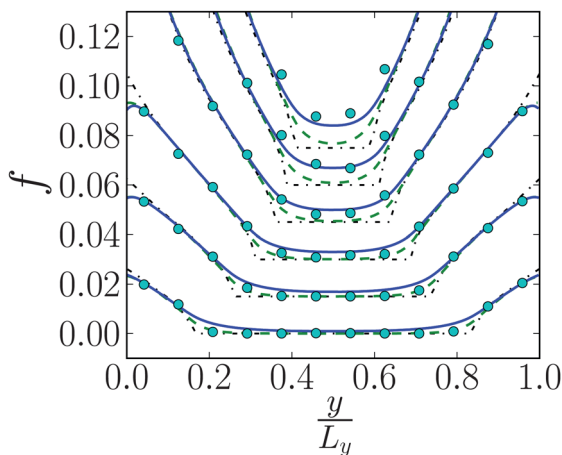


Fig. 10 Fluidity profiles for $N_y = 12$, for $\sigma_w = 0.20, 0.28, 0.36, 0.48, 0.60, 0.72$ in model units. Filled circles: numerical results, dashed green line: solution of eqn (14) with $\xi(\dot{\gamma}) = 0.03702$, solid blue line: solution of eqn (14) with $\xi(\dot{\gamma}) = 0.01146\dot{\gamma}^{-0.25}$. The thin dash-dotted lines represent the bulk fluidity f_{bulk} . Note that the curves are shifted with respect to each other for clarity.

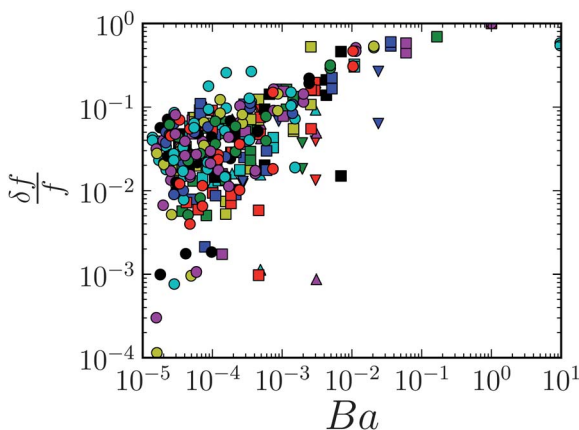


Fig. 11 Relative deviations $\frac{\delta f}{f}$ of the local fluidity f from the bulk fluidity $f_{\text{bulk}}(\sigma)$ measured in the simulations, where σ is the local shear stress, as a function of the estimated Babel number $Ba = \left(\xi_0 \frac{\nabla \sigma}{\sigma - \sigma_d} \right)^2$. We have set ξ_0 to 0.037 (see Fig. 10). Data only include regions where $\sigma > \sigma_d$, but cover various applied pressures and channel widths: (∇) 6 blocks, (\blacktriangle) 10 blocks, (\blacksquare) 16 blocks, (\bullet) 24 blocks.

4.3 Shear rate fluctuations in the plug

Quite recently, Jop *et al.*⁴⁵ have showed experimentally that the seemingly quiescent plug in the centre of the microchannel actually sustains finite shear rate fluctuations. This observation is obviously consistent with the occurrence of sparse plastic events in the plug in our simulations.

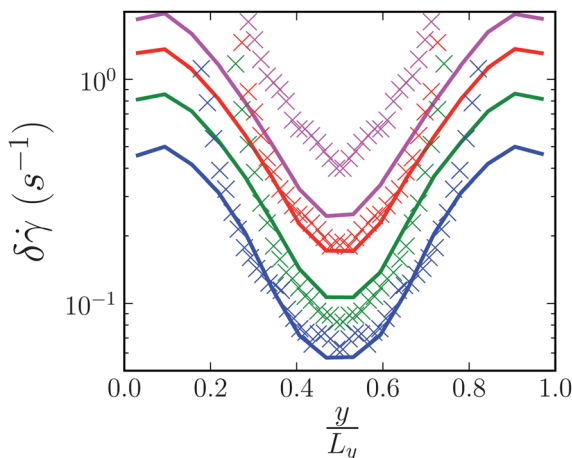


Fig. 12 Shear rate fluctuations $\delta\dot{\gamma}(y)$ (averaged along the x -direction), for $\sigma_w = 141$ Pa, 188 Pa, 235 Pa, 282 Pa (identical to Fig. 6), from bottom to top. Experimental data collected by Jop *et al.* (\times),⁴⁵ numerical results for $N_y = 16$ (solid lines).

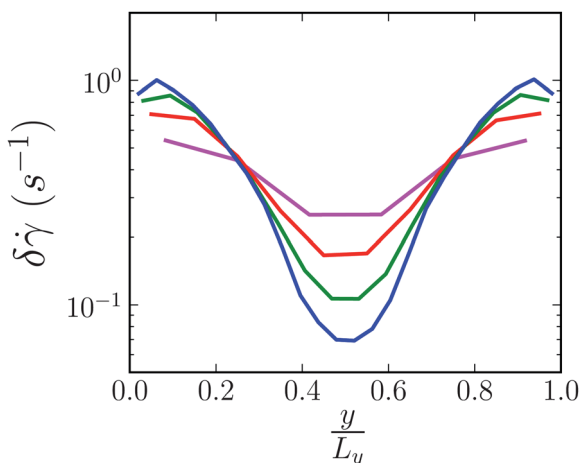


Fig. 13 Shear rate fluctuation profiles for a given stress at the wall, $\sigma_w = 0.48$ in model units, for different channel widths: (fuchsia) 6, (red) 10, (green) 16, and (blue) 24 blocks, in descending order of minimal values.

To go further than this qualitative agreement, we have directly compared the local shear rate fluctuations $\delta\dot{\gamma}(x, y) = \sqrt{\langle \dot{\gamma}(x, y)^2 \rangle - \langle \dot{\gamma}(x, y) \rangle^2}$ to the experimental data,[¶] with the parameters used to fit the associated velocity profiles (see Fig. 9). Here, $\dot{\gamma}(x, y)$ is the local shear rate at point (x, y) ; it is given by $\dot{\gamma}(x, y) = 2(\dot{\epsilon}_{xy}^{\text{pl}}(x, y) + \dot{\epsilon}_{xy}^{(1)}(x, y))$ in the model and is therefore obtained directly, that is, without deriving the velocity with respect to space. Fig. 12 presents the experimental shear

[¶] Note that we have discarded the two curves corresponding to the lowest applied pressures, which seem to plateau in the centre, because we were not entirely sure of the accuracy of these measurements.

rate fluctuation profiles and their numerical counterparts for $N_y = 16$ blocks crosswise. A semi-quantitative agreement is observed in regions far from the walls – apart from the large discrepancy at the highest applied pressure. The discrepancies in the highly-sheared regions near the walls will be considered below. It is interesting to note that the fitted channel size provides another estimate for the size N_ϕ of an elastoplastic block, which agrees with the first one, $N_\phi \approx 2$. Fig. 13 shows the dependence of the shear rate fluctuations on the channel size for a given stress at the wall. As expected from the expression of the Babel number, the fluctuations in the plug decay when the channel width is increased.

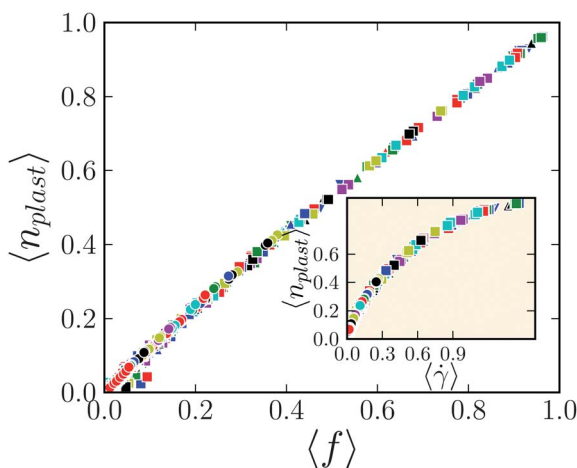


Fig. 14 Time-averaged fraction of plastic blocks $\langle n_{\text{plast}} \rangle$ on a given streamline as a function of the mean fluidity $\langle f \rangle$ on that line, for diverse applied pressures and various channel widths: (\blacktriangledown) 6 blocks, (\blacktriangle) 10 blocks, (\blacksquare) 16 blocks, (\bullet) 24 blocks. Inset: $\langle n_{\text{plast}} \rangle$ vs. the mean shear rate $\langle \dot{\gamma} \rangle$ on the line. (Same symbols).

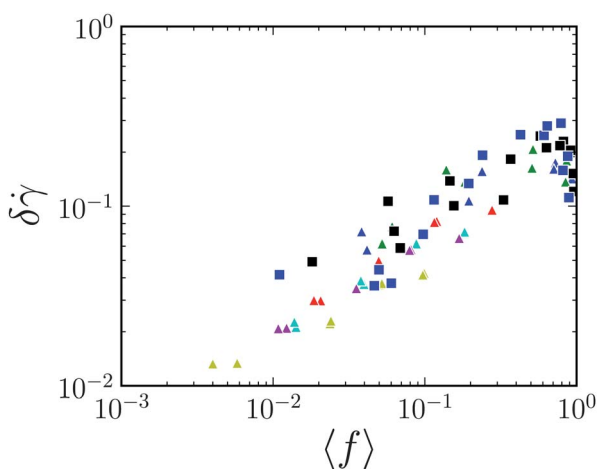


Fig. 15 Shear rate fluctuations $\delta \dot{\gamma}$ on a given streamline as a function of the mean fluidity $\langle f \rangle$ on that line, for diverse applied pressures and various channel widths: (\blacktriangle) 8 blocks, (\blacksquare) 16 blocks, (\bullet) 24 blocks.

Let us note that the data collected by Jop and co-workers suggest a proportionality between the shear rate fluctuations and the local fluidity, implying that both are indicators of the intensity of the plastic activity. Fig. 14 shows that the line-averaged plastic activity does indeed depend linearly on the local fluidity in our channel flow simulations, despite some discrepancies at low values of the fluidity, that is, probably in the plug. However, the relation between the shear rate fluctuations and the mean fluidity is much less clear (see Fig. 15).

5 A specific rheology near the walls?

In the previous section, we have dealt with the flow cooperativity associated with the coupling of heterogeneous streamlines, leaving aside another potentially significant difference with the bulk homogeneous flow: the presence of walls bounding the flow, which is known to affect the flow of diverse complex fluids like wormlike micellar solutions,^{54,55} laponite,⁵⁶ dense colloidal suspensions,⁴⁷ *etc.* Indeed, Goyon *et al.* provided experimental evidence of the occurrence of ample changes when rough walls are substituted for smooth walls.³⁹ Then, much larger deviations from bulk rheology are observed, especially at high applied pressures, and these deviations are maximal close to the walls, contrary to the predictions based on the Babel number.

5.1 Weak deviations due to the no-slip boundary condition

Remember that walls are described by a no-slip boundary condition in our model. This condition results in a significantly larger dissipation during plastic events in their vicinity. Is this sufficient to capture the very large deviations observed experimentally?

Fig. 16 shows the local flow curve for the simulations. To decouple to a certain extent the problem of wall rheology from the inhomogeneous driving, the latter being associated with large values of Ba , a relatively large channel is considered here. For each value of the wall stress, the points with the highest local shear rates in Fig. 16 are closest to the walls. We do observe some slight deviations,^{||} but they are clearly much weaker than in Goyon's observations (see Fig. 6 of ref. 44 for instance). In this respect, they much better describe the situation for smooth walls, which, at first, might seem surprising given the no-slip boundary condition. Yet, in reality, the large slip observed at the smooth walls is not expected to give rise to significant changes: it only adds a simple global translation to the complex velocity field obtained with the no-slip boundary condition.

5.2 Physical effect of rough walls

As the deviations observed for rough walls are not captured by a simple no-slip boundary condition, we discuss here some physical mechanisms that may be responsible for the observed behaviour.

^{||} Nevertheless, replacing the no-slip boundary condition with a periodic boundary condition will play a role if the Babel number is large enough. See ref. 40 for the effect of confinement on the observed yield stress in a bi-periodic Poiseuille flow.

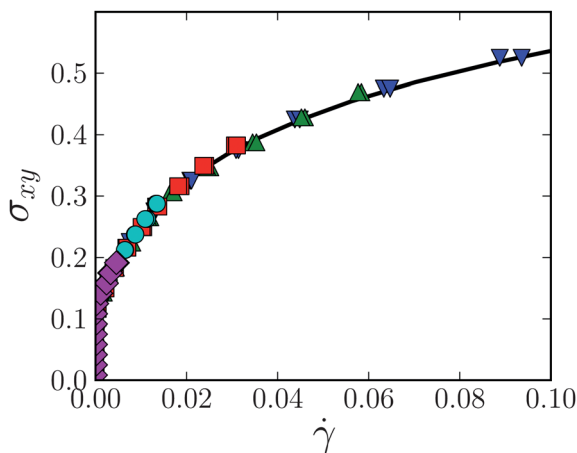


Fig. 16 Local shear stress as a function of the local shear rate, for various applied pressures for a channel width of 24 blocks. The corresponding stresses at the walls are: (purple rhombs) $\sigma_w = 0.2$; (cyan dots) $\sigma_w = 0.2$; (red squares) $\sigma_w = 0.4$; (green upper triangles) $\sigma_w = 0.5$; (blue lower triangles) $\sigma_w = 0.6$.

First, the static structure near the walls is known to differ from that in the bulk. For smooth, or not too rough, boundaries, stratification in layers is often reported over a distance of a few particle diameters,^{57,58} though not systematically: Goyon *et al.*⁴⁴ actually observed no such layering in their experiments. Besides, the vicinity of a solid boundary hinders the mobility of Brownian particles.⁵⁹ But these structural changes for the material at rest imply a decrease of the fluidity at the wall, as opposed to the enhancement that is experimentally observed by Goyon³⁹ and Geraud⁴⁶ at high enough stresses, *i.e.*, where the largest deviations occur. Alternatively, the specific behaviour at the wall is often rationalised by the existence of a depleted ‘lubrication layer’ close to the wall, as is often found in sheared dispersions.^{60–66} This phenomenon is more acute for deformable particles⁶² undergoing high shear rates and/or high shear gradients; it generates an apparent wall slip. However, at the very high concentrations investigated here, owing to the large osmotic pressure, such a lubricating layer would have a thickness of the order of 100 nm or less^{44,65,66} (if the lubricating layer is composed of pure solvent). Effectively, Goyon directly measured the concentration profile across the channel and was not able to detect any significant variation. This finding was corroborated by the absence of radial droplet migration for a similar material in a Taylor–Couette cell, even at high shear rates, as reported by Ovarlez *et al.*⁵³ Adding the fact that systems of soft particles have a much weaker viscosity dependence on concentration than their hard particle counterparts, the effects of concentration variations could be ruled out as regarded in Goyon’s experiments. Nevertheless, we attempted to simulate a less viscous layer close to the wall by decreasing the yield stress of the associated mesoscopic blocks, but this only had little effect on the rest of the system. Therefore, one is led to seek another explanation.

An aspect that has been overlooked so far is the reported observation of wall slip in Goyon’s, Geraud’s and Jop and Mansard’s works,^{39,44,46,58} both with smooth

and rough walls. In order to extract information that is relevant for the bulk flow, the authors measured the local velocities and shear rates in the channel by microscopic observation, so that the occurrence of slippage should *a priori* not affect their results. Indeed, in the presence of smooth surfaces, where wall slip accounts for around 30% of the maximal velocity at the typical pressures applied by Goyon *et al.*,³⁹ slip only results in a global translation of the system, that leaves the local flow curve strictly unaltered. For rough surfaces, let us first remark that the presence of wall slip is more surprising, since roughened surfaces** are often used to strongly suppress, or eliminate, the slip for the very same type of materials, which is monitored by rheological measurements, and then used as benchmarks for a system without slip.^{61,64,67–69} However, in several cases, the measurement of local velocities in the flow, either by microvelocimetry with fluorescent tracers^{44,46,70} or through direct visualisation with confocal microscopy,^{45,58} demonstrated that concentrated emulsions may slip along rough surfaces in microchannels. A seemingly quadratic,^{46,70} or linear,⁵⁸ dependence of the slip velocity on the shear stress at the wall was reported in these cases. As a side note, let us add that slip along a rough wall is not restricted to the microchannel geometry: for instance, Divoux *et al.* showed with ultrasonic speckle velocimetry that another yield stress fluid, namely carbopol, experiences a phase of total slip in a Taylor–Couette rheometer whose cylinders had been coated with sand paper.⁷¹

Now, when particles slide along a rough wall, they are expected to bump into, and be deformed by, the surface asperities. In the case of asperities that are large as compared to the “particle” size (~ 60 microns *vs.* from a few to 20 microns), this phenomenon is best exemplified by the spatio-temporal diagram acquired with ultrasonic velocimetry for a carbopol microgel, Fig. 6 of ref. 72, where one can see a large deformation of the material that originates at the rotor and propagates almost instantaneously into the bulk; this signal was interpreted by the authors as the signature of a “bump” into a surface protuberance. Albeit less visible, this effect should also appear with walls characterised by a smaller roughness, whereby rough walls in the presence of slip act as sources of mechanical noise and cause deviations from bulk rheology in their vicinity. This tentative scenario has the potential to explain why deviations may, or may not, be observed in the vicinity of rough surfaces: for instance, Goyon *et al.*⁴⁴ and Ovarlez *et al.*,⁵³ as well as Seth *et al.*,⁷³ have reported that the local flow curves obtained in wide-gap Taylor–Couette or plate–plate geometries with rough walls could be mapped onto the macroscopic flow curves; yet, they also indicated that, in those cases, no evidence of wall slip could be found. Very recently, Mansard endeavoured to investigate the impact of wall roughness by combining experiments and molecular dynamics simulations.⁵⁸ Non-monotonic variations of the wall fluidity as a function of the roughness were reported in the experiments, but the data did not allow for the extraction of the parameters responsible for the deviations from macroscopic rheology. Nevertheless, he noted that “the particles must jump over the patterns [on the walls]. This effect induces the rearrangements and increases the wall fluidity”.

** Diverse methods are available for roughening a surface, such as sandblasting, covering it with sandpaper, or coating it with particles.

Naturally, this prompts the following question: what determines the occurrence of slip along rough walls? This question lies far beyond the scope of the present study. Let us simply note that in ref. 39, 44–46 the size of surface asperities was a couple of microns at most, that is, significantly less than the typical “particle” size, which plausibly favours slip, as well as the high shear rates experienced at the microchannel walls. Nevertheless, recent theories of slip along smooth walls involved, in addition, parameters such as the deformability of the droplets,^{63,64} and the particle–wall interactions,⁷⁴ not to mention the presumably significant impact of Brownian motion in cases where it is relevant.^{75,76} As far as we know, the somewhat daunting challenge to extend these theories to the case of rough walls still awaits a successful accomplisher.

In the above discussion, we have carefully eluded the question of the surface's chemistry and its interactions with the particles. However, Seth *et al.* showed that they can play a significant role; in particular, for the yield stress fluid they studied, smooth attractive surfaces were observed to induce deviations from macroscopic rheology relatively far into the bulk, whereas smooth repulsive surfaces induced none at all.

Finally, we would like to mention another possible impact of the confinement of the material between walls. The channel may be so narrow that the layers where the specific wall rheology dominates start overlapping. This situation, which is described as strong confinement, is expected to occur when the channel width becomes of the order of, or smaller than, the cooperativity length ξ . For the data of ref. 39, 44, 45 discussed above, this mechanism is therefore not relevant.

5.3 Fictitious plastic events along the wall as mechanical noise sources

As we have already noted, non-local effects leading to deviations from the macroscopic flow curve are often rationalised in terms of the fluidity diffusion equation, eqn (14) (see, *e.g.*, ref. 39, 40, 44–46, 52, 58, 73). In this approach, the fluidity at the wall is needed as an input parameter, whose precise value turns out to be determinant. Most likely, the suggested mechanical noise at the walls would be hidden in that value. (Note that, in Goyon's report⁷⁰ the fluidity at the rough walls, where larger deviations are observed, is indeed larger than that for smooth walls and larger than the bulk fluidity corresponding to the same shear stress.)

Our mesoscopic model is also oblivious to the microscopic details of the flow near a boundary and therefore cannot describe the effect of wall slip along a rough wall without further input. Nevertheless, since bumps act as sources of mechanical noise in the system, one can attempt to account for their occurrence by adding fictitious plastic events along the walls. Note that this *ad hoc* treatment is similar to imposing a wall fluidity larger than the bulk fluidity as a boundary condition when solving the fluidity diffusion equation, eqn (14).

More precisely, we have modified the implementation of the model slightly, so that a wall is now described as a line of plastically inert blocks: the bottom wall will, for instance, occupy the portion of space $0 \leq y \leq 1$, and the no-slip boundary condition is imposed at its centre, *i.e.*, $y = 0.5$. On this line, a fraction of blocks

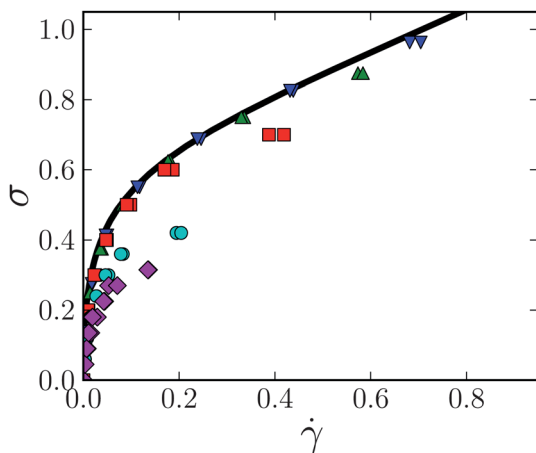


Fig. 17 Local shear rate $\sigma(y)$ vs local shear rate $\dot{\gamma}(y)$ (averaged on streamlines $y = \text{cst}$) in the micro-channel, when fictitious mechanical noise sources of intensity $\dot{\epsilon}_{xy}^{\text{fict pl}} = \pm 4.5$ are added on a fraction (1/3) of blocks on the wall lines. $\sigma_w = (\blacklozenge)$ 0.36, (\bullet) 0.48, (\blacksquare) 0.8, (\blacktriangle) 1.0, (\blacktriangledown) 1.1 in model units. Solid line: macroscopic flow curve.

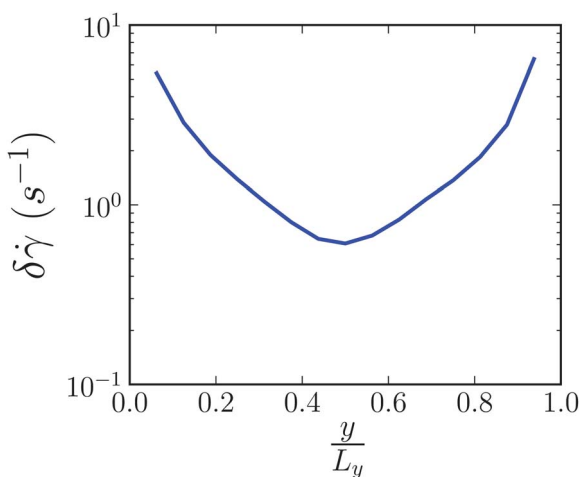


Fig. 18 Shear rate fluctuation profiles in the presence of fictitious plastic events along the walls. A third of the blocks on the wall lines have been randomly selected to release a constant plastic stress $\dot{\sigma}_{xy}^{\text{pl fict}} = 4.5$ per unit time.

was selected^{††} at random to act as sources of mechanical noise, that is, to mimic, *e.g.*, bumps of particles into surface asperities. To do so, they shall release a constant plastic strain $\dot{\epsilon}_{\text{fict}}^{\text{pl}}$ per unit time, along the direction of the macroscopic shear (for simplicity). We emphasise that the mechanical equilibrium is not violated by the addition of these fictitious plastic events.

^{††} Note that shuffling these blocks, *i.e.*, selecting new random blocks as noise sources, at low enough frequency, hardly affects the results presented below.

Fig. 17 shows the local flow curves obtained with this protocol. The observed deviations are qualitatively similar to those reported by Goyon (see Fig. 7 of ref. 44). However, we must note that a rather intense mechanical noise is required to get such deviations ($\dot{\epsilon}_{\text{fict}}^{\text{pl}} \approx 5$). (As the value of $\dot{\epsilon}_{\text{fict}}^{\text{pl}}$ is arbitrary, we do not seek quantitative agreement with the experimental data here.) In addition, these fictitious plastic events also alter the shear rate fluctuation profile, as shown in Fig. 18. Besides a global increase of the fluctuations, the profile no longer flattens in the vicinity of the walls, which renders it more consistent with the experimental results of Jop *et al.* (collected in a channel with rough walls).

6 Conclusions and outlook

In conclusion, we have derived analytical formulae from continuum mechanics for the effect and time evolution of a plastic event occurring in a two dimensional medium bounded by walls. We have integrated these formulae in a lattice model for the flow of amorphous solids, in which elastoplastic blocks receive stress from their surroundings and have a certain probability to become plastic; the chosen form of probabilities for the onset and end of a plastic event allowed us to match experimental flow curves for concentrated emulsions. Then, we turned to the simulation of flow in microchannels, where the most prominent feature is the existence of a seemingly unsheared “plug”. Remarkable manifestations of spatial cooperativity in the flow had been unveiled experimentally, and we have proposed to distinguish those pertaining to cooperativity in the bulk from those pointing to the specific rheology near a solid boundary. For the former category, deviations of time-averaged quantities are generally weak, but could nevertheless be observed with our model. More strikingly, shear rate fluctuations were observed in the plug, consistent with the experiments. With regard to the specific wall rheology, it turned out that imposing a no-slip boundary condition at the walls in our model was not sufficient to capture the experimentally observed phenomena. We have discussed several possible physical origins for the departure from the observed macroscopic behaviour, above all, in the vicinity of rough surfaces; we have insisted in particular on a tentative scenario in which mechanical noise is created at the wall by, *e.g.*, bumps of particles into surface asperities as they slide along the wall. Finally, an *ad hoc* implementation of this mechanical noise was attempted.

Concerning our mesoscopic model, several improvements can be considered. First and foremost, regions undergoing plastic events are fluidised, and the presence of fluid-like regions is expected to damp shear waves and reduce the cooperativity. This point is not taken into account in the model. Also, the distinction between an activation temperature, of non-cooperative origin, and a more general effective temperature will be worth investigating further, both for thermal and ‘athermal’ soft solids under shear. In an unrelated way, it has been made apparent that, in spite of the vast amount of literature on the question of slip for soft solids and the recent progress made in that respect,⁶³ the issue of slip along rough surfaces and its consequences on the local fluidity remain quite challenging.

Appendices

A Derivation of the correction terms to the propagator for a system bounded by walls

The system covers the domain $(x, y) \in [0, L_x] \times [-L_y, L_y]$ and is periodically replicated throughout space. The region $y \in [0, L_y]$, bounded by walls at $y = 0$ and $y = L_y$ represents the real system, whereas the other half is a fictitious region introduced for the calculations.

For any plastic event $\varepsilon^{\text{pl}} = (\varepsilon_{xx}^{\text{pl}}, \varepsilon_{xy}^{\text{pl}})^T$ occurring at position (x, y) in the real half, a 'symmetric' plastic event $\varepsilon^{\text{pl}'} = (\varepsilon_{xx}^{\text{pl}}, -\varepsilon_{xy}^{\text{pl}})^T$ is created at location $(x, -y)$ in the fictitious region. For symmetry reasons, the y -component of the velocity field is thereby cancelled on lines $y = 0$ and $y = L_y$ (bear in mind that the $2L_y$ -wide system is periodically replicated).

Let us now introduce forces $f_x^{(y=0)}$ and $f_x^{(y=L_y)}$ along the x -direction at the bottom ($y = 0$) and top ($y = L_y$) walls, respectively, to cancel the x -components. The Fourier transform of the force field reads:

$$f_x(m, n) = f_x^{(y=0)}(m) + (-1)^n f_x^{(y=L_y)}(m)$$

Note that we have simplified the notations by using the shorthand $g(m, n)$ for $\hat{g}(p_m, q_n)$, for any function g , where $p_m \equiv \frac{2\pi m}{L_x}$ and $q_n \equiv \frac{2\pi n}{L_y}$ are the Fourier wavenumbers.

With these forces, the Fourier-transformed displacement field turns into:

$$u^{(1)}(m, n) = \mathcal{G}^\infty(m, n) \cdot (\hat{\varepsilon}^{\text{pl}}(m, n) + \hat{\varepsilon}^{\text{pl}'}(m, n)) + O(m, n) \cdot f_x(m, n) \quad (15)$$

$$\equiv u^{*\infty}(m, n) + u^{\text{corr}}(m, n), \quad (16)$$

where \hat{u}^{corr} is the contribution from the wall forces and \hat{O} is the Oseen-Burgers tensor introduced in eqn (8). The star in $\hat{u}^{*\infty}$ only indicates that this symbol represents the velocity field induced by both the real plastic event and its 'symmetric' counterpart.

Remarking that the condition of zero velocity at the bottom and top walls reads, in terms of the Fourier components,

$$\forall m, \sum_n u^{(1)}(m, n) = 0$$

$$\text{and } \forall m, \sum_n (-1)^n u^{(1)}(m, n) = 0,$$

respectively, we obtain two equations on the f_x after insertion from eqn (15). Adding and subtracting these equations yield, for any m :

$$\sum_{n \in \mathbb{O}} u_x^{*\infty}(m, n) + O(m, n) \cdot \left(\left(\hat{f}_x^{(y=0)} - \hat{f}_x^{(y=L_y)} \right)(m) \right) = 0$$

$$\sum_{n \in E} u_x^{*\infty}(m, n) + O(m, n) \cdot \left(\left(\hat{f}_x^{(y=0)} + \hat{f}_x^{(y=L_y)} \right) (m) \right) = 0$$

where $O \equiv 2\mathbb{Z} + 1$ is the set of odd integers, and $E \equiv 2\mathbb{Z}$ is the set of even integers.

The solution of this linear system of equations is:

$$f(m \neq 0, n \in \delta) = \frac{-\mu}{e_\delta(m)} \sum_{n' \in \delta} u_x^{*\infty}(m, n'), \quad (17)$$

where the symbol δ stands for either E (even n 's) or O (odd n 's). The expressions for $m = 0$ are written separately:

$$f(0, n \in 2\mathbb{Z}) = 0$$

$$f(0, n \in O) = \frac{-4\mu}{L_y^2} \sum_{n' \in O} u_x^{*\infty}(m, n').$$

In eqn (17), we have introduced auxiliary functions $e_E(m)$ and $e_O(m)$, which satisfy:^{††}

$$e(m) \equiv \sum_{n \in \mathbb{Z}} \frac{q_n^2}{(p_m^2 + q_n^2)^2} = \frac{L_y^2}{2\pi} \left[\frac{-\pi}{\sinh^2(2\pi L_y m / L_x)} + \frac{L_x}{2m L_y} \frac{1}{\tanh(2\pi L_y m / L_x)} \right]$$

$$e_E(m) \equiv \sum_{n \in E} \frac{q_n^2}{(p_m^2 + q_n^2)^2} = \frac{1}{4} e\left(\frac{m}{2}\right)$$

$$e_O(m) \equiv \sum_{n \in O} \frac{q_n^2}{(p_m^2 + q_n^2)^2} = e(m) - \frac{1}{4} e\left(\frac{m}{2}\right)$$

Now, the infinite summation in eqn (17) needs to be calculated. For a single plastic event located at (x_{ev}, y_{ev}) , that is, $\hat{\varepsilon}^{pl}(m, n) = e^{-ip_m x_{ev}} e^{-iq_n y_{ev}} (\hat{\varepsilon}_{xx}^{pl}, \hat{\varepsilon}_{xy}^{pl})^T$, the use of the expression for $\hat{u}_x^{*\infty}$ leads to:

$$\sum_{n' \in \delta} \hat{u}_x^{*\infty}(m, n') = 4e^{-ip_m x_{ev}} \left[\varepsilon_{xy}^{pl} \left(p_m \frac{2L_y^3}{\pi^3} j_\delta(X) - \frac{L_y}{\pi} k_\delta(X) \right) - 2i\varepsilon_{xx}^{pl} p_m \frac{L_y^2}{\pi^2} s_\delta(X) \right], \quad (18)$$

where the δ -subscript stands for either E or O , and $X \equiv (x, \alpha) \equiv \left(\frac{\pi y_{ev}}{L_y}, \frac{p_m L_y}{\pi} \right)$.

Inserting eqn (18) into eqn (17), summing the plastic activity of all y lines, *i.e.*, $y = 0.5, \dots, L_y - 0.5$ ($L_y \in \mathbb{N}^*$) in the discretised version, and Fourier transforming the results along the x -direction *via* the operator \mathcal{F}_x , defined by $\mathcal{F}_x \sigma = \frac{1}{L_x} \int \sigma(x) e^{-ip_m x} dx$, one finally arrives at:

^{††} The analytical calculations leading to the second part of the equality involve the decomposition into simple elements and the use of well established summation results.⁷⁷

^{§§} The +0.5 term comes from the fact that the y -coordinate of a block (of unit size) is evaluated at its centre.

$$\hat{\underline{u}}^{corr}(m, n \in \delta) = \begin{pmatrix} \frac{-4q_n^2}{4\mu q^4} \cdot \left[\sum_y \underbrace{\left(\frac{p_m^2 L_y^2}{e_\delta(m) \pi^3} j_\delta(X) - \frac{1}{\pi} k_\delta(X) \right)}_{\equiv \zeta_\delta(X)} \mathcal{F}_x \sigma_{xy}^{pl}(m, y) - 2i \sum_y \underbrace{\left(\frac{p_m L_y}{e_\delta(m) \pi^2} s_\delta(X) \right)}_{\equiv \zeta_\delta(X)} \mathcal{F}_x \sigma_{xx}^{pl}(m, y) \right] \\ \frac{4p_m q_n}{4\mu q^4} \left[\sum_y \left(\frac{p_m^2 L_y^2}{e_\delta(m) \pi^3} j_\delta(X) - \frac{1}{\pi} k_\delta(X) \right) \mathcal{F}_x \sigma_{xy}^{pl}(m, y) - 2i \sum_y \frac{p_m L_y}{e_\delta(m) \pi^2} s_\delta(X) \mathcal{F}_x \sigma_{xx}^{pl}(m, y) \right] \end{pmatrix},$$

where new summations appear and can be expressed analytically *via* a decomposition into simple elements and the use of known summation formulae:⁷⁷

$$j(x, \alpha) \equiv \sum_{k=-\infty}^{+\infty} \frac{k \sin(kx)}{(k^2 + \alpha^2)^2} = \frac{\pi}{2\alpha^2} \frac{\sinh(\alpha(\pi - x))}{\sinh(\alpha\pi)} - \frac{1}{2\alpha^2} \mathcal{H}(x, \alpha)$$

$$j_E(x, \alpha) = \frac{1}{8} j\left(2x, \frac{\alpha}{2}\right)$$

$$\mathcal{H}(x \neq 0, \alpha) \equiv \sum_{k=-\infty}^{+\infty} \frac{k \sin(kx)}{(k - i\alpha)^2} = \frac{h(x, \alpha) + h(x, -\alpha)}{2}$$

$$h(x \neq 0, \alpha) \equiv -i \sum_{k=-\infty}^{+\infty} \frac{k \exp(ikx)}{(k - i\alpha)^2} = \frac{\pi \exp(-x\alpha)}{1 - \cosh(2\pi\alpha)} [x\alpha(e^{2\pi\alpha} - 1) + 2\pi\alpha - (e^{2\pi\alpha} - 1)]$$

$$k(x, \alpha) \equiv \sum_{k=-\infty}^{+\infty} \frac{k^3 \sin(kx)}{(k^2 + \alpha^2)^2} = \frac{\pi \sinh(\alpha(\pi - x))}{2 \sinh(\alpha\pi)} + \frac{\mathcal{H}(x, \alpha)}{2}$$

$$k_E(x, \alpha) = \frac{1}{2} k\left(2x, \frac{\alpha}{2}\right)$$

$$s(x, \alpha) \equiv \sum_{k=-\infty}^{+\infty} \frac{k^2 \exp(ikx)}{(k^2 + \alpha^2)^2} = \frac{\pi \cosh(\alpha(\pi - x))}{2 \alpha \sinh(\alpha\pi)} + \frac{\pi}{4} u(x, \alpha)$$

$$s_E(x, \alpha) = \frac{1}{4} s\left(2x, \frac{\alpha}{2}\right)$$

$$u(x, \alpha) \equiv \frac{2x \cosh(\alpha(x - 2\pi)) + (2\pi - x) \cdot 2 \cosh(\alpha x)}{(1 - \cosh(2\pi\alpha))}$$

The function j_O is obtained by writing $j(x, \alpha) = j_O(x, \alpha) + j_E(x, \alpha)$; the same applies for the other functions with subscripts O.

The coincidence of the infinite summations and their analytical expressions has been verified numerically for particular values of the parameters.

As a technical remark, we would like to mention that the preceding formulae are difficult to evaluate numerically for $|\alpha| \gg 1$, on account of the large arguments of the hyperbolic functions. Nevertheless, the following approximations provide very satisfactory results in the limit of large α ($\alpha > 0$):

$$\frac{\sinh[\alpha(\pi - x)]}{\sinh(\alpha\pi)} \approx \exp(-x\alpha) - \exp(\alpha(x - 2\pi))$$

$$\frac{\cosh[\alpha(\pi - x)]}{\sinh(\alpha\pi)} \approx \exp(-x\alpha) + \exp(\alpha(x - 2\pi))$$

$$h(x, \alpha) \approx -2\pi \exp(-x\alpha)[x\alpha - 1]$$

$$u(x, \alpha) \approx -2[x \exp[\alpha(x - 4\pi)] + x \exp(-\alpha x) + (2\pi - x) \cdot \exp[\alpha(x - 2\pi)]]$$

Our final result is:

$$\begin{pmatrix} \sigma_{xx}^{\text{corr}}(m, n) \\ \sigma_{xy}^{\text{corr}}(m, n) \end{pmatrix} = \begin{pmatrix} \frac{-2p_m q_n^2}{\underline{q}^4} \left[i \sum_y \zeta_\delta(X) \mathcal{F}_x \sigma_{xy}^{\text{pl}}(m, y) + 2 \sum_y \xi_\delta(X) \mathcal{F}_x \sigma_{xx}^{\text{pl}}(m, y) \right] \\ \frac{q_n(p_m^2 - q_n^2)}{\underline{q}^4} \left[i \sum_y \zeta_\delta(X) \mathcal{F}_x \sigma_{xy}^{\text{pl}}(m, y) + 2 \sum_y \xi_\delta(X) \mathcal{F}_x \sigma_{xx}^{\text{pl}}(m, y) \right] \end{pmatrix}, \quad (19)$$

where we should note that $\zeta(0, n \in \mathbb{O}) = \frac{-2}{L_y^2}$.

As a computational detail, note that the y -coordinates are here integers shifted by half unity, *i.e.*, of the form $p + \frac{1}{2}$, $p \in \mathbb{N}$, whereas computational routines for Fast Fourier Transforms take as input an array with integer indices. It is therefore easier to suppose that the walls are at positions $y = -\frac{1}{2}$ and $y = L_y - \frac{1}{2}$. This translation is readily achieved by simply multiplying the Fourier components of the correction term, as given above, by prefactors $\exp\left(\frac{iq_n}{2}\right)$.

Assuming a complexity $O(N \ln N)$ for the Fast Fourier Transform of an array of N cells, the number of operations performed at each time step of our algorithm is of order $O(L_x L_y^2 \ln L_x)$ for large integers L_y and L_x , as it is evident from eqn (19).

B Calculation of the line-averaged velocity

The mean velocity on a line $y = y_0$ reads:

$$\begin{aligned} \langle u_x \rangle_x(y_0) &\equiv \frac{1}{L_x} \int_{-L_x/2}^{L_x/2} u_x(x, y_0) dx \\ &= \sum_{n=-\infty}^{+\infty} \hat{u}_x^*(m=0, n) e^{iq_n y_0} \\ &= \sum_{\substack{n=-\infty \\ n \neq 0}}^{+\infty} \hat{u}_x^{*\infty}(0, n) e^{iq_n y_0} + \hat{u}_x^{*\infty}(0, 0) - (1 - 2|y_0|/L_y) \sum_I \hat{u}_x^{*\infty}(0, \cdot) + \sum_P \overbrace{\hat{u}_x^{\text{corr}}(0, \cdot)}^0 e^{iq_n y_0} \\ &= \sum_{y_{\text{ev}}} \frac{a}{2\mu} \left[\text{sign}(y_0 - y_{\text{ev}}) \cdot \left(1 - \frac{|y_0 - y_{\text{ev}}|}{L_y} \right) + 1 - \frac{y_{\text{ev}}}{L_y} - \frac{y_0}{L_y} \right] \mathcal{F}_x \sigma_{xy}^{\text{pl}}(m=0, y_{\text{ev}}), \end{aligned}$$

where the last summation is performed over all streamlines y_{ev} , and $\hat{u}_x^{*\infty}$ is the bulk contribution in the duplicated system.

C Estimation of the deviations due to bulk cooperativity

Assume the fluidity diffusion equation is a valid approximation,

$\xi^2 \Delta f - (f - f_{\text{bulk}}) = 0$ where $f = \frac{\dot{\gamma}}{\sigma}$ is the local fluidity, and ξ is a cooperativity length that may vary with the shear rate.

Let $\delta f = f - f_{\text{bulk}}$ be the deviation from the expected fluidity profile owing to cooperative effects between regions subject to different driving forces.

One now assumes $\delta f \ll f_{\text{bulk}}$ and $\Delta \delta f \ll \Delta f_{\text{bulk}}$.

To leading order, the fluidity diffusion equation reads

$$\xi^2 \Delta f_{\text{bulk}} = \delta f.$$

The amplitude of the deviations due to cooperativity is given by the Babel number $\text{Ba} \equiv \frac{\delta f}{f} \approx \xi^2 \frac{\Delta f_{\text{bulk}}}{f_{\text{bulk}}}$

If the flow curve follows a Herschel–Bulkley law: $\sigma(\dot{\gamma}) = \sigma_d + A \dot{\gamma}^n$, $f'_{\text{bulk}} = \frac{\sigma'^2}{A^n}$

$$\times \frac{\sigma^{n-1}(\sigma - \sigma_d)^{\frac{1}{n}-1}}{n} \left[\left(\frac{1}{n} - 1 \right) \frac{\sigma^{-n}}{\sigma - \sigma_d} \left((1-n) + n \frac{\sigma_d}{\sigma} \right)^2 - n \sigma^{-n-1} \left(1 - n + (1+n) \frac{\sigma_d}{\sigma} \right) \right]$$

Here, the primes denote derivatives with respect to the space coordinate. Then,

$$\frac{f''_{\text{bulk}}}{f_{\text{bulk}}} = \frac{\sigma'^2}{n(\sigma - \sigma_d)} \left[\left(\frac{1}{n} - 1 \right) \frac{\sigma^{-n}}{\sigma - \sigma_d} \left((1-n) + n \frac{\sigma_d}{\sigma} \right)^2 - \frac{n}{\sigma} \left(1 - n + (1+n) \frac{\sigma_d}{\sigma} \right) \right]$$

To leading order, one finally arrives at $\frac{\delta f}{f} \sim \xi^2 \frac{\sigma'^2}{(\sigma - \sigma_d)^2}$.

Acknowledgements

We thank T. Divoux, K. Martens, P. Chaudhuri, S. Manneville, and M. Fardin for interesting discussions. JLB is supported by Institut Universitaire de France and by grant ERC-2011-ADG20110209.

References

- 1 L. Berthier, G. Biroli, J.-P. Bouchaud, L. Cipelletti, D. El Masri, D. L'Hôte, F. Ladieu and M. Pierno, *Science*, 2005, **310**, 1797–800.
- 2 C. Heussinger, P. Chaudhuri and J.-L. Barrat, *Soft Matter*, 2010, **6**, 3050–3058.
- 3 D. Rodney, A. Tanguy and D. Vandembroucq, *Modell. Simul. Mater. Sci. Eng.*, 2011, **19**, 083001.
- 4 K. A. Dahmen, Y. Ben-Zion and J. T. Uhl, *Nat. Phys.*, 2011, **7**, 554–557.
- 5 A. Argon and H. Kuo, *Mater. Sci. Eng.*, 1979, **39**, 101–109.
- 6 A. Lemaître and C. Caroli, *Phys. Rev. E: Stat., Nonlinear, Soft Matter Phys.*, 2007, **76**, 036104.
- 7 M. Tsamados, A. Tanguy, F. Léonforte and J.-L. Barrat, *Eur. Phys. J. E*, 2008, **26**, 283–93.
- 8 M. Falk and J. Langer, *Phys. Rev. E: Stat. Phys., Plasmas, Fluids, Relat. Interdiscip. Top.*, 1998, **57**, 7192.
- 9 M. L. Falk and J. S. Langer, *Annual Review of Condensed Matter Physics*, vol 2, 2011, vol. 2, pp. 353–373.
- 10 P. Sollich, F. Lequeux, P. Hébraud and M. Cates, *Phys. Rev. Lett.*, 1997, **78**, 2020–2023.
- 11 P. Sollich, *Phys. Rev. E: Stat. Phys., Plasmas, Fluids, Relat. Interdiscip. Top.*, 1998, **58**, 738.
- 12 P. Hébraud and F. Lequeux, *Phys. Rev. Lett.*, 1998, **81**, 2934–2937.
- 13 P. Coussot, Q. Nguyen, H. Huynh and D. Bonn, *Phys. Rev. Lett.*, 2002, **88**, 175501.

- 14 M. Manning, J. Langer and J. Carlson, *Phys. Rev. E: Stat., Nonlinear, Soft Matter Phys.*, 2007, **76**, 056106.
- 15 S. M. Fielding, M. E. Cates and P. Sollich, *Soft Matter*, 2009, **5**, 2378.
- 16 L. Bocquet, A. Colin and A. Ajdari, *Phys. Rev. Lett.*, 2009, **103**, 036001.
- 17 K. Chen, P. Bak and S. Obukhov, *Phys. Rev. A: At., Mol., Opt. Phys.*, 1991, **43**, 625–630.
- 18 V. V. Bulatov and A. S. Argon, *Modell. Simul. Mater. Sci. Eng.*, 1994, **2**, 167–184.
- 19 V. V. Bulatov and A. S. Argon, *Modell. Simul. Mater. Sci. Eng.*, 1994, **2**, 185–202.
- 20 V. V. Bulatov and A. S. Argon, *Modell. Simul. Mater. Sci. Eng.*, 1994, **2**, 203–222.
- 21 J.-C. Baret, D. Vandembroucq and S. Roux, *Phys. Rev. Lett.*, 2002, **89**, 195506.
- 22 G. Picard, A. Ajdari, F. Lequeux and L. Bocquet, *Phys. Rev. E: Stat., Nonlinear, Soft Matter Phys.*, 2005, **71**, 010501.
- 23 E. R. Homer and C. A. Schuh, *Acta Mater.*, 2009, **57**, 2823–2833.
- 24 K. Martens, L. Bocquet and J.-L. Barrat, *Soft Matter*, 2012, **8**, 4197.
- 25 K. Martens, L. Bocquet and J.-L. Barrat, *Phys. Rev. Lett.*, 2011, **106**, 156001.
- 26 A. Nicolas and J.-L. Barrat, *Phys. Rev. Lett.*, 2013, **110**, 138304.
- 27 H. Princen, *J. Colloid Interface Sci.*, 1985, **105**, 150–171.
- 28 C. Maloney and A. Lemaitre, *Phys. Rev. E: Stat., Nonlinear, Soft Matter Phys.*, 2006, **74**, 016118.
- 29 A. Amon, V. Nguyen, A. Bruand, J. Crassous and E. Clément, *Phys. Rev. Lett.*, 2012, **108**, 135502.
- 30 M. Le Merrer, S. Cohen-Addad and R. Höhler, *Phys. Rev. Lett.*, 2012, **108**, 188301.
- 31 J. Bouchaud and E. Pitard, *Eur. Phys. J. E: Soft Matter Biol. Phys.*, 2001, **6**, 231–236.
- 32 M. Cloitre, R. Borrega, F. Monti and L. Leibler, *Phys. Rev. Lett.*, 2003, **90**, 068303.
- 33 G. Picard, A. Ajdari, F. Lequeux and L. Bocquet, *Eur. Phys. J. E*, 2004, **15**, 371–81.
- 34 F. Leonforte, R. Boissière, A. Tanguy, J. Wittmer and J.-L. Barrat, *Phys. Rev. B: Condens. Matter Mater. Phys.*, 2005, **72**, 224206.
- 35 P. Schall, D. A. Weitz and F. Spaepen, *Science*, 2007, **318**, 1895–9.
- 36 J. Bokeloh, S. V. Divinski, G. Reglitz and G. Wilde, *Phys. Rev. Lett.*, 2011, **107**, 235503.
- 37 R. Besseling, L. Isa, P. Ballesta, G. Petekidis, M. Cates and W. Poon, *Phys. Rev. Lett.*, 2010, **105**, 268301.
- 38 M. Talamali, V. Petäjä, D. Vandembroucq and S. Roux, *C. R. Mec.*, 2012, **340**, 275.
- 39 J. Goyon, A. Colin, G. Ovarlez, A. Ajdari and L. Bocquet, *Nature*, 2008, **454**, 84–7.
- 40 P. Chaudhuri, V. Mansard, A. Colin and L. Bocquet, *Phys. Rev. Lett.*, 2012, **109**, 036001.
- 41 O. Pouliquen, Y. Forterre and S. Le Dizes, *Advances in Complex Systems*, 2001, **04**, 441–450.
- 42 R. R. Hartley and R. P. Behringer, *Nature*, 2003, **421**, 928–31.
- 43 A. Amon, R. Bertoni and J. Crassous, *Phys. Rev. E*, 2013, **87**, 012204.
- 44 J. Goyon, A. Colin and L. Bocquet, *Soft Matter*, 2010, **6**, 2668.
- 45 P. Jop, V. Mansard, P. Chaudhuri, L. Bocquet and A. Colin, *Phys. Rev. Lett.*, 2012, **108**, 148301.
- 46 B. Geraud, L. Bocquet and C. Barentin, *Eur. Phys. J. E*, 2013, **36**, 9845.
- 47 L. Isa, R. Besseling and W. C. K. Poon, *Phys. Rev. Lett.*, 2007, **98**, 198305.
- 48 L. Isa, R. Besseling, A. Morozov and W. Poon, *Phys. Rev. Lett.*, 2009, **102**, 058302.
- 49 O. Pouliquen and R. Gutfraind, *Phys. Rev. E: Stat. Phys., Plasmas, Fluids, Relat. Interdiscip. Top.*, 1996, **53**, 552.
- 50 R. Gutfraind and O. Pouliquen, *Mech. Mater.*, 1996, **24**, 273–285.
- 51 J.-B. Salmon, L. Bécu, S. Manneville and A. Colin, *Eur. Phys. J. E*, 2003, **10**, 209–221.
- 52 K. Kamrin and G. Koval, *Phys. Rev. Lett.*, 2012, **108**, 178301.
- 53 G. Ovarlez, S. Rodts, A. Ragouilliaux, P. Coussot, J. Goyon and A. Colin, *Phys. Rev. E: Stat., Nonlinear, Soft Matter Phys.*, 2008, **78**, 036307.
- 54 C. Masselon and A. Colin, *Phys. Rev. E: Stat., Nonlinear, Soft Matter Phys.*, 2010, **81**, 021502.
- 55 L. Bécu, S. Manneville and A. Colin, *Phys. Rev. Lett.*, 2004, **93**, 018301.
- 56 T. Gibaud, C. Barentin and S. Manneville, *Phys. Rev. Lett.*, 2008, **101**, 258302.
- 57 P. Ballesta, R. Besseling, L. Isa, G. Petekidis and W. Poon, *Phys. Rev. Lett.*, 2008, **101**, 258301.
- 58 V. Mansard, PhD thesis, Université de Bordeaux I, 2012.
- 59 E. Pagac, R. Tilton and D. Prieve, *Chem. Eng. Commun.*, 1996, **148**, 105–122.
- 60 A. Yoshimura and R. K. Prud'homme, *J. Rheol.*, 1988, **32**, 53.
- 61 H. A. Barnes, *J. Non-Newtonian Fluid Mech.*, 1995, **56**, 221–251.
- 62 J. Franco, C. Gallegos and H. Barnes, *J. Food Eng.*, 1998, **36**, 89–102.
- 63 S. Meeker, R. Bonnecaze and M. Cloitre, *Phys. Rev. Lett.*, 2004, **92**, 198302.
- 64 S. P. Meeker, R. T. Bonnecaze and M. Cloitre, *J. Rheol.*, 2004, **48**, 1295.
- 65 J.-B. Salmon, A. Colin and S. Manneville, *Phys. Rev. Lett.*, 2003, **90**, 228303.
- 66 L. Bécu, P. Grondin, A. Colin and S. Manneville, *Colloids Surf., A*, 2005, **263**, 146–152.

- 67 T. Mason, J. Bibette and D. Weitz, *J. Colloid Interface Sci.*, 1996, **179**, 439–448.
- 68 M. Sanchez, C. Valencia, J. Franco and C. Gallegos, *J. Colloid Interface Sci.*, 2001, **241**, 226–232.
- 69 G. H. Meeten, *J. Non-Newtonian Fluid Mech.*, 2004, **124**, 51–60.
- 70 J. Goyon, PhD thesis, Université de Bordeaux I, 2008.
- 71 T. Divoux, C. Barentin and S. Manneville, *Soft Matter*, 2011, **7**, 9335–9349.
- 72 T. Divoux, C. Barentin and S. Manneville, *Soft Matter*, 2011, **7**, 8409–8418.
- 73 J. R. Seth, C. Locatelli-Champagne, F. Monti, R. T. Bonnecaze and M. Cloitre, *Soft Matter*, 2012, **8**, 140.
- 74 J. R. Seth, M. Cloitre and R. T. Bonnecaze, *J. Rheol.*, 2008, **52**, 1241.
- 75 R. Besseling, L. Isa, E. R. Weeks and W. C. Poon, *Adv. Colloid Interface Sci.*, 2009, **146**, 1–17.
- 76 P. Ballesta, G. Petekidis, L. Isa, W. C. K. Poon and R. Besseling, *J. Rheol.*, 2012, **56**, 1005.
- 77 I. Gradshteyn and I. Ryzhik, *Tables of Integrals, Series and Products*, (edited by A. Jeffrey), 1994.